Journal of Physics:
Condensed Matter

TOPICAL REVIEW • OPEN ACCESS

Microscopic origins of electron trapping in amorphous silicon nitride (*a*-Si_3N_4) and its role in charge-trap flash memory

To cite this article: Christoph Wilhelmer *et al* 2026 *J. Phys.: Condens. Matter* **38** 333002

Journal of Physics: Condensed Matter

OPEN ACCESS

RECEIVED
15 May 2026

REVISED
3 July 2026

ACCEPTED FOR PUBLICATION
15 July 2026

PUBLISHED
17 August 2026

TOPICAL REVIEW

Microscopic origins of electron trapping in amorphous silicon nitride (a-Si_3N_4) and its role in charge-trap flash memory

Christoph Wilhelmer[1,*], **Lukas Hückmann**[2,*], **Jonathon Cottom**[2,3,4], **Dominic Waldhoer**[1], **Jörg Meyer**[2] and **Tibor Grasser**[1]

[1] Institute for Microelectronics, TU Wien, Vienna, Austria
[2] Leiden Institute of Chemistry, Leiden University, Leiden, The Netherlands
[3] Advanced Research Center for Nanolithography, Amsterdam, The Netherlands
[4] Institute for Theoretical Physics, University of Amsterdam, Amsterdam, The Netherlands
[*] Authors to whom any correspondence should be addressed.

E-mail: wilhelmer@iue.tuwien.ac.at and l.huckmann@lic.leidenuniv.nl

Keywords: amorphous silicon nitride, charge trapping, computational modeling, defects, charge capture cross section, charge-trap flash memory

Abstract

Amorphous silicon nitride (a-Si_3N_4) is widely used as the charge storage layer of charge-trap flash (CTF) memory devices, where its high density of deep localized electronic states enables long-term data retention at room temperature. Despite its technological relevance, the microscopic nature of the charge traps in a-Si_3N_4 is still controversial. In recent years, atomistic modeling has enabled the characterization of intrinsic defects in a-Si_3N_4, providing new insights into their structural and electronic properties that are comprehensively discussed in this review. We demonstrate that a variety of structural irregularities, including over- and undercoordinated atoms, Si—Si bonds, vacancies and strained Si—N bonds, introduce localized electronic states in the amorphous network, which act as precursor sites for trapping and retaining electrons. The associated charge transition processes at these trapping sites are analyzed within the framework of nonradiative multiphonon theory and evaluated in the context of macroscopic CTF functionality. Additionally, we present a density functional theory-based computational approach to estimate electron capture cross sections of intrinsic defect sites in a-Si_3N_4.

Contents

1. Introduction

Silicon nitride (Si_3N_4) is a ubiquitous dielectric distinguished by its exceptional thermal, chemical, and mechanical stability [1–8], making it an indispensable material in advanced silicon-based device fabrication, where thin amorphous silicon nitride films (a-Si_3N_4) are routinely incorporated into complementary metal-oxide-semiconductor architectures. In these devices, a-Si_3N_4 films can function as gate spacers, sidewall isolation layers, etch-resistant hard masks, and durable passivation coatings that shield device surfaces from environmental degradation and ionic diffusion [9–15]. Beyond microelectronics, silicon nitride has emerged as a key material in photonic integrated circuits (PICs) [16–20], as a potential anode material in conversion-type lithium ion batteries [21–30], and as a mechanical resonator used in quantum cavity optomechanical devices, or nanomechanical sensors [31–33].

Among its various applications, a-Si_3N_4 plays a particularly important technological role as the charge storage layer in charge-trap flash (CTF) memory. CTF technology has largely superseded floating-gate memory due to its superior leakage control and reliability at the nanoscale, providing the scalability required for densely stacked device architectures [34, 35]. The success of CTF is rooted in the exceptional charge-trapping capability of silicon nitride, facilitated by a high density of deep electron traps ($> 10^{19}\,\mathrm{cm}^{-3}$) [36–42], enabling extrapolated charge retention times approaching 10 years at 150 °C [43–45]. To meet the increasing demand for data storage capacity, which has been further driven by the expansion of artificial intelligence architectures, a fundamental understanding of the microscopic origins of charge trapping is necessary to continue device scaling. However, experimental characterization of these trapping sites remains challenging due to the amorphous nature of silicon nitride thin films and the associated broad distribution of defect properties. Consequently, the microscopic nature of the charge traps remains a subject of active debate.

To gain deeper insight into the underlying mechanisms, considerable efforts have been made by various research groups over the last years to model amorphous silicon nitrides using atomistic methods. In particular, the electronic structure of a-Si_3N_4 has been investigated in great detail using first-principles methods such as density functional theory (DFT) [30, 46–58]. These studies suggest that the random network in the amorphous structure of silicon nitride thin films gives rise to a remarkably broad variety of possible charge trapping centers. This is because, in contrast to for example a-SiO_2 [59, 60], a-Si_3N_4 has a considerable fraction of over- and undercoordinated atoms when compared to its crystalline counterparts [61]. On top of common impurities such as O [62], Ti [63] or B [64], these structural defects introduce localized electronic states which facilitate the localization of charge carriers [48, 49, 53, 57, 65]. Similarly, Si–Si bonds [55–57, 66, 67] and even fully coordinated Si with strained Si–N bonds [51–53] have been proposed as suitable electron traps. Furthermore, hydrogen, which is inevitably incorporated in a-Si_3N_4 thin films during growth, gives rise to additional H-related charge trapping centers [52, 54].

In addition to analyzing structural and electronic properties of defects, DFT is also a powerful tool for characterizing the structural response upon charge trapping and the stability of a trapped charge state. For the case of deep level defects in semiconductors and insulators, it has been shown that hybrid DFT can capture charge transition probabilities with high accuracy, allowing for the evaluation of charge

capture coefficients, defect levels, and line shape functions of charge traps, including the zero-phonon lines, solely by means of first-principle calculations [68, 69]. Besides basic defect characterizations in semiconductors and insulators, this methodology has also been employed to describe stochastic charge trapping processes in metal-oxide-semiconductor field effect transistors (MOSFETs) [60, 70]. However, in contrast to MOSFETs, where the trapping of electrons from the substrate at defects in the amorphous dielectric poses a significant reliability problem [71–73], the trapping of electrons from the substrate in the nitride layer is the fundamental mechanism to enable data storage in flash memories.

1.1. Outline of the review

In this topical review, we provide a comprehensive discussion of insights from recent studies on the structural and electronic properties of a-Si_3N_4. Our discussion aims to shed light on the microscopic origins of the outstanding charge trapping capabilities of silicon nitrides as utilized in non-volatile memory devices. We characterize the properties of structural defects in a-Si_3N_4 and propose a methodology to evaluate the electron capture properties of these defects. In the introductory section 2, we briefly discuss how electron localization in a-Si_3N_4 is used to store information in CTF devices. Section 3 is dedicated to the chemistry of silicon nitride, particularly on how it is fabricated, how its properties can be fine-tuned, and its structural features on the microscopic level. These experimental observations serve as a reference for the computational models introduced in section 4, where modeling techniques and the electronic structure obtained from first-principles are discussed.

Building on this, the nonradiative multiphonon (NMP) model to describe electron capture at defect sites from conduction band states is outlined in section 5 and we describe how the corresponding defect parameters can be obtained with DFT. In section 6, we use the NMP framework to assess the charge trapping energetics of various defect sites discussed in the literature. To complement the review of previous literature, this manuscript presents new first-principles calculations in section 6.4. Specifically, we evaluate the electron capture cross sections of representative intrinsic defects within NMP, utilizing the mobility edge of a-Si_3N_4 as the initial state of the charge transition. Based on these calculations, we argue that electron capture at this defect type is governed by a small classical energy barrier at room temperature, while thermal emission is strongly suppressed. In section 6.5, we compare the first-principles evaluations of electron traps with insights from experiment and device-scale simulations. Additionally, we discuss the role of the common impurities hydrogen and oxygen in charge trapping. Finally, we give a short outlook and perspective on remaining open questions in section 7.

2. Data storage in CTF devices

A CTF device allows for the storage of information by localizing and retaining charge carriers from the substrate at specific atomic sites in the storage layer. The most basic CTF design is comprised of a (poly-)silicon-oxide-nitride-oxide-silicon (SONOS) stack as illustrated in figure 1(a). The tunneling oxide (silicon dioxide) is employed to control the electron migration between the substrate (silicon) and the nitride during operation, while the blocking oxide (silicon dioxide) prevents the charges in the nitride layer to escape to the metallic gate (polycrystalline silicon), thereby enabling long-term retention. Over the last decades, significant efforts have been devoted to develop new technologies to enhance the performance of CTF. This includes, for example, TANOS stacks, where tantalum nitride (TaN) is employed to improve the gate control, while alumina (Al_2O_3) substitutes silica as the blocking oxide to improve the data retention [74]. Additionally, more sophisticated structures such as band gap engineered SONOS (BE-SONOS), where an additional ONO stack is integrated between the silicon-oxide interface, have been demonstrated to modulate the tunneling barrier, thereby suppressing direct tunneling at low electric fields [75, 76]. For the sake of simplicity, we will focus our discussion on SONOS in this work.

The CTF device is operated in three distinct cycles: program, erase and read. Initially, in an unbiased device, no charge carriers are trapped from the channel in the storage layer, which corresponds to a logic 1 state of the device. In this state, the device can be turned on by applying a gate voltage above the low initial threshold voltage $V_{\mathrm{th}}^{\mathrm{i}}$, which is called the program cycle of the device. The effects of the positive gate bias on the band diagram of a SONOS device is schematically shown in figure 1(a) [77]. Due to the large electric field in the device, the electronic band edges of the insulator tilt towards a lower energy. When the positive gate voltage is sufficiently large ($\sim$10 MV cm^{-1}) [78, 80, 81], electrons from the substrate can tunnel through the tunneling oxide into the nitride. This elastic tunneling process through the triangular potential barrier of the oxide is typically described by Fowler–Nordheim tunneling.

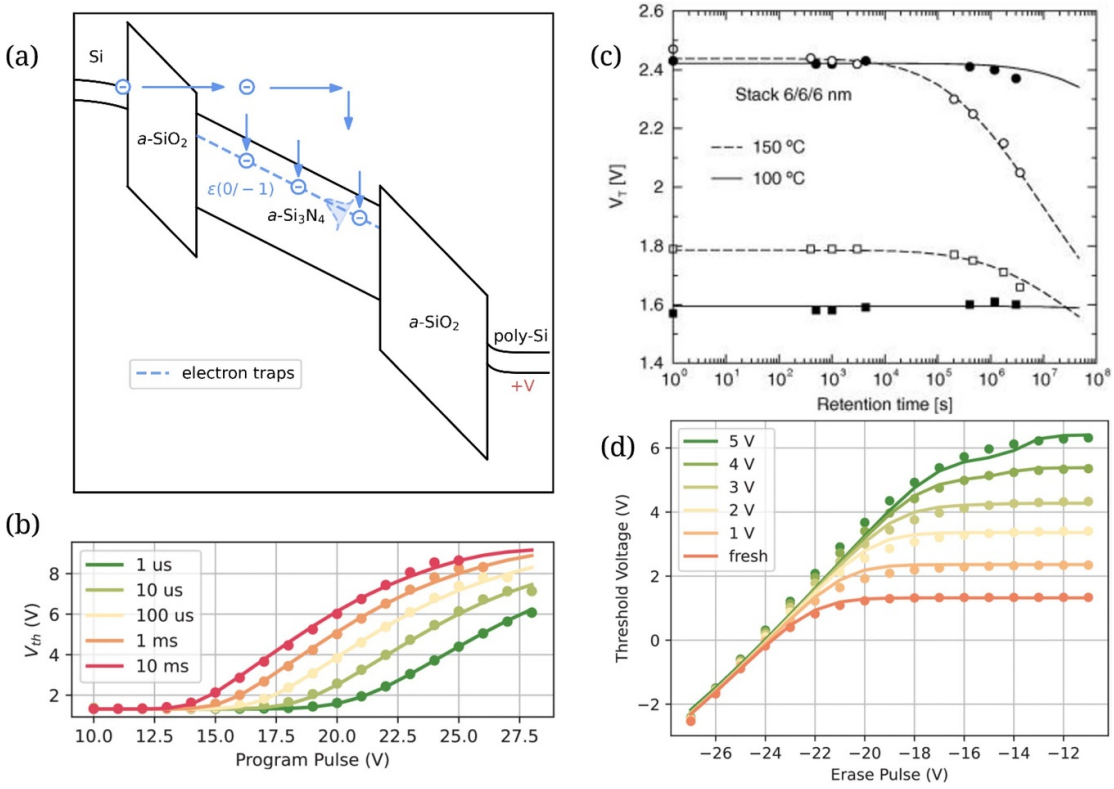

Figure 1. (a) Schematic band diagram of a SONOS device during the program cycle with a positive applied gate bias. (b) Threshold voltage of a planar SONOS device as a function of the program pulse for different program pulse widths. Data points are electrical measurements, while the lines represent TCAD simulations of the process. Reproduced with permission from [78]. © 2023 The Authors. CC BY-NC-ND 4.0. (c) Extrapolation times of a SONOS at 100 °C and 150 °C for two different initial threshold voltages. Reprinted from [79], Copyright (2008), with permission from Elsevier. (d) Threshold voltage as a function of the erase pulse voltage for different initial program states. Reproduced with permission from [78]. © 2023 The Authors. CC BY-NC-ND 4.0.

If the electrons are not captured by defects at the Si/SiO_2 interface [82] or inside the SiO_2 tunneling oxide [60], they are injected into the Si_3N_4 conduction band. Due to the high kinetic energy of the injected electrons, they migrate through the nitride layer where they lose energy through scattering events. This causes the carriers to relax toward lower-energy delocalized states near the mobility edge of the conduction band, where they transition to a localized state at a suitable trapping site [78, 83]. Due to the inherent structural disorder of amorphous thin films, the associated trapping states are not discrete, but rather their energies are distributed across a broad spectrum within the band gap, as indicated by the Gaussian-like distribution around the electron trapping level. The thermalization and migration process results in the majority of electrons getting trapped behind the tunneling oxide-nitride interface and accumulate near the blocking oxide interface [37, 78, 84, 85], as for example observed in the trap density profile obtained with trap spectroscopy by charge injection and sensing (TSCIS) (shown also in figure 10(c) [37]). Technology computer-aided design (TCAD) simulations suggest that electrons near the tunneling oxide-interface are more likely to be lost to the channel by trap-to-band tunneling [78, 86]. Consequently, a high trapped electron density further away from this interface is considered beneficial for charge retention. While the migration of electrons from these trapping sites toward the gate is theoretically possible, this leakage is suppressed by the thick blocking oxide, which reduces the tunneling rate to the gate.

The presence of localized charges in the nitride layer substantially alters the electrostatics of the device, because electrons from the substrate are repelled by the negative electric field of the trapped electrons. At the device level, this manifests as an increase of the threshold voltage to $V_{\mathrm{th}}^{\mathrm{f}}$. The shift of V_{th} with positive gate bias is shown in figure 1(b), where the threshold voltage as a function of the program pulse is measured (data points) and simulated (full lines) for different pulse widths [78]. The change of the threshold voltage results in a change of the logic state of the device to 0. In the absence of an external bias, the oxides on both sides of the storage layer prevent charge escape, enabling reliable data retention even when the device is powered off. The retention characteristics of a SONOS device at elevated

temperatures are shown in figure 1(c) for two different initial threshold voltages [79]. At 100 °C, the programmed V_{th} only changes slightly even after 10^7 s. In contrast, at 150 °C, V_{th} begins to decrease already after 10^5 s, which is attributed to thermionic emission and trap-to-band tunneling [78]. At room temperature, however, V_{th} of the same device remained practically constant with time, demonstrating excellent long-term retention capabilities even for basic SONOS stacks [79].

It should be noted that lateral migration of trapped charge carriers can introduce significant reliability issues in CTFs due to fluctuating threshold voltages. In particular, the retention performance in dense three-dimensional architectures like 3D-NAND flash memories is known to be negatively affected by lateral migration mechanisms [87, 88]. Moreover, during the program cycle, trapped electrons can be partially emitted due to the high electric field and laterally migrate through the nitride layer [39, 81, 89, 90].

The logic state of the device can be probed during the read cycle by sensing the channel conductivity under applied reference voltages. Early implementations of flash memories relied on binary Single-Level Cell storage, where a single reference voltage V_{read} between the V_{th} of a programmed and an erased cell ($V_{th}^{i} < V_{read} < V_{th}^{f}$) is applied. If the trapping layer is empty, the applied V_{read} is high enough to create a conductive channel, allowing current to flow through the bit line. Conversely, if electrons are trapped in the nitride layer, the transistor remains off with applied V_{read}, preventing current flow and identifying the logic state as 0. Modern high-density 3D NAND flash technologies predominantly utilize multi-level cell technologies, where the total V_{th} window is partitioned into 2^n distinct threshold voltage distributions, where n is the number of bits stored per cell. While this architecture allows for a higher information storage density, the device also becomes more sensitive to bit errors induced by microscopic charge redistributions or loss within the trapping layer.

Finally, the logic state of the device can be reset during the erase cycle by applying a negative gate bias. This negative bias facilitates the removal of electrons from the nitride back to the substrate and, simultaneously, can lead to the injection and localization of holes [91–94], thereby resetting the logic state. The decrease of the threshold voltage as a function of the negative gate voltage (erase pulse) of a planar SONOS device is shown in figure 1(d) [78]. In this plot, the voltages in the legend correspond to different ΔV_{th} targets to which the devices were previously programmed.

3. The chemistry of silicon nitride

Silicon nitride occurs in both crystalline and amorphous phases, each offering distinct physical properties and technological utilities. While the amorphous phase allows for variable stoichiometry, the crystalline forms are restricted to a stoichiometric Si:N ratio of 3:4. Understanding the structural differences between these two forms is essential, as the transition from long-range crystalline order to the amorphous state, i.e., short-range order with long-range disorder, fundamentally impacts the nature of the charge-trapping sites.

3.1. Crystalline Si_3N_4

For Si_3N_4, three distinct crystalline phases have been reported (α, β, γ). The α- and β-phases crystallize in a trigonal and hexagonal unit cell, respectively ($P31c$, $P6_3/m$, see table 1) [96, 118, 119]. Both crystal structures are comprised of corner-linked SiN_4 tetrahedra, with each N atom adopting a trigonal-planar configuration (NSi_3).

α-Si_3N_4 is prone to impurities (primary C and O) and transforms irreversibly to the β-phase upon annealing above 1500 °C [120]. Furthermore, the heat of formation for this conversion scales with impurity concentration, approaching 0 kJ mol^{-1} for nearly phase-pure samples [121]. These findings, combined with the structural similarity of the phases differing primarily by a mirror plane, have sparked a debate regarding whether the α-phase is a unique modification or merely an inverted AB$\bar{A}\bar{B}$ stack of the β-Si_3N_4 structure [95]. The γ-phase is a more recently discovered cubic high-pressure modification, for which practical applications are not identified yet [97, 98, 122].

According to DFT calculations, the nitrogen vacancy (V_N) in β-Si_3N_4 is a deep trap that triggers the formation of an Si−Si bond upon electron localization [66, 123–127]. However, growing phase-pure crystalline phases is challenging in practice [128, 129]. If the growing process is not controlled carefully, crystalline silicon nitride forms nanocrystallites that are often embedded within an amorphous matrix and consequently, material properties are frequently compromised by an abundance of grain boundaries [105, 130–132]. For this reason, charge trapping in phase-pure crystals cannot be distinguished

Table 1. Key properties of crystalline α-, β-, and γ-phase as well as amorphous a-Si_3N_4 including the space group, crystal system, lattice constants a, c, the density ρ, the bulk modulus B, and the band gap E_g.

	α-Si_3N_4		β-Si_3N_4		γ-Si_3N_4		a-Si_3N_4	
space group	$P31c$	[95]	$P6_3/m$	[96]	$Fd\bar{3}m$	[97]	—	
cryst. system	trigonal	[95]	hexagonal	[96]	cubic	[98]	—	
a (Å)	7.55	[95]	7.60	[95]	7.73	[97]	—	
c (Å)	5.62	[95]	2.91	[95]	—		—	
ρ (g cm^{-3})	3.15	[96]	3.20	[96]	3.75	[97]	2.6 – 3.0	[99]
B (GPa)	240	[100]	259	[101]	290	[102]	150 – 180	[103]
E_g (exp.) (eV)	∼5.00[a]	[104]	∼5.00[a]	[105]	5.05	[106]	4.2 – 5.4	[107]
E_g (PBE[b]) (eV)	4.7 – 4.8	[108, 109]	4.3 – 4.5	[108–110]	3.4 – 3.6	[108, 111]	3.5 – 4.3	[48]
E_g (hybrid) (eV)	5.37	[112]	5.3	[113]	4.80	[114]	3.5 – 5.0	[53, 65]

[a] α- and β-Si_3N_4 are difficult to grow phase-pure and have an indirect optical band gap. Therefore, literature sources are not consistent and probably affected by varying degrees of defects. Quantum chemical calculations [110, 115] and UV absorption measurements on low-defect a-Si_3N_4 [116] indicate the actual band gap is between 5 eV to 6 eV.

[b] GGA functionals are known to systematically underestimate band gaps [114, 117]. The listed values vary slightly across the literature depending on the exact settings (supercell size, pseudo potentials, etc).

from trapping at grain boundaries, amorphous domains etc. Thus, the lack of experimental accessibility, combined with the difficulties in crystal growth, currently renders crystalline silicon nitride unsuitable for use in memory devices.

3.2. Amorphous SiN_x

For technological applications, amorphous silicon nitride (a-SiN_x) is the preferred form due to its favorable chemical, optical, and electrical properties, combined with its relative ease of fabrication. Usually, a-SiN_x is employed as a thin film, which can readily be grown on Si-wafers and other substrates, allowing its usage in a wide range of architectures. To this end, several growth protocols have been developed that affect the properties of the film and must therefore be taken into account when a-SiN_x is used as a charge-trapping medium.

3.2.1. Thin film growth and fine-tuning

a-SiN_x films are commonly grown via chemical vapor deposition (CVD), where volatile gaseous precursors react at elevated temperatures forming a solid film on a surface of a substrate. Typical precursor combinations include silane (SiH_4) or dichlorosilane (SiH_2Cl_2), which decompose at high temperatures between 700 °C – 900 °C and condense with N_2 or ammonia (NH_3) on the substrate forming a solid a-SiN_x film [133–136].

In similar fashion, atomic layer deposition (ALD) relies on sequential, self-limiting surface reactions to achieve layer-by-layer film growth [137, 138]. In each cycle, the substrate is alternately exposed to a silicon precursor and a nitrogen source, separated by purge steps, enabling precise control of film thickness and composition. These processes yield high-quality, low-stress films with near-stoichiometric composition and angstrom-level thickness control. In particular, ALD provides excellent conformality on high-aspect-ratio structures, making it well suited for complex three-dimensional device architectures [139–141]. Nevertheless, the relatively low growth per cycle and, in some cases, elevated thermal requirements mean that CVD methods remain attractive for high-throughput industrial fabrication [142, 143].

Both CVD and ALD can be performed at elevated temperature at low pressure (LP) or plasma enhanced (PE), where the exact route has a significant impact on the result. LP-CVD and -ALD yield smoother films with good control over the hydrogen content and film stoichiometry. However, LP protocols provide slow growth rates and require high temperatures, which constrains the thermal budget when integrating LP-CVD a-SiN_x in device architectures containing temperature sensitive materials. PE variants mitigate both limitations as plasma-activated species grow faster at lower temperatures (≈300 °C to 400 °C) [134], though lead to substantial incorporation of hydrogen, increasing the porosity and lowering the density. For these reasons, PE-grown films usually require post-deposition annealing.

A third technique is radiofrequency (RF) magnetron sputtering, where energetic ions (commonly Ar^+) bombard a silicon target, ejecting atoms that subsequently react with nitrogen and deposit on the substrate to form a-SiN_x [144, 145]. This technique requires only low processing temperatures, enableshydrogen-free deposition (given that the Ar/N_2 is free of impurities), and considerable flexibility in tuning film composition and properties through parameters such as substrate temperature, nitrogen

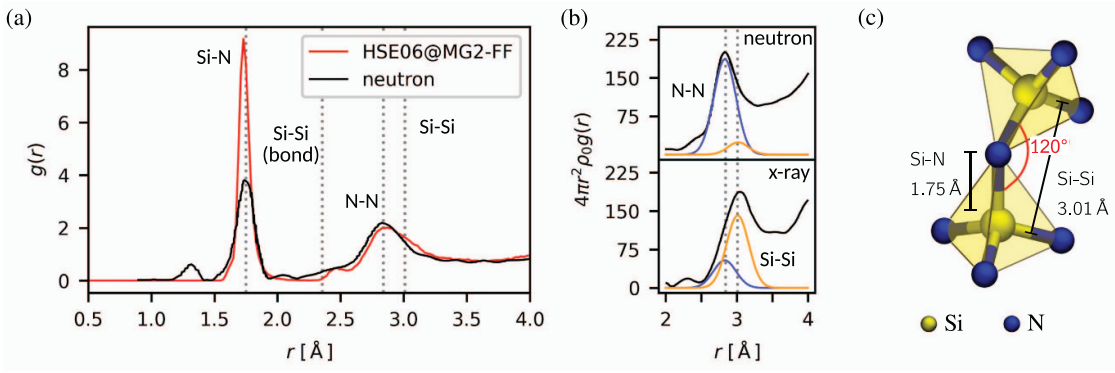

Figure 2. (a) The pair distribution function $g(r)$ determined from neutron diffraction measurements [165] and from structures generated with the MG2 force field with subsequent optimization at the HSE06 hybrid-DFT level (see section 4) [53]. For comparison, the Si−N nearest neighbor distance, the Si−Si bond length, the N−N second-nearest neighbor distance, and the Si−Si second-nearest neighbor distance are added. (b) $g(r)$ in the range $2\,\text{Å} < r < 4\,\text{Å}$ determined from neutron [165] and x-ray diffraction [61] with the respective fits for the N−N and Si−Si second-nearest neighbor distribution. Reprinted from [165], Copyright (1979), with permission from Elsevier. (c) Illustration of two corner-linked SiN_4 tetrahedra with the Si−N bond length, the Si−N−Si bond angle, and the Si−Si second-nearest neighbor distance.

partial pressure and flow rate [146], RF power [147], and chamber pressure [148]. However, sputtering is inherently a line-of-sight deposition technique, which limits film conformality on substrates with complex topography or high aspect-ratio structures [149].

The deposition techniques described above allow to systematically tune the structural and electronic properties of a-SiN_x films through variations in process parameters, e.g., the process temperature [150], deposition rate, gas phase composition [151], and annealing. Additionally, the composition of the reactant gas mixture plays a central role, as it directly determines the resulting film stoichiometry. Nitrogen-rich conditions in the gas phase ($N/Si > 4$) yield near-stoichiometric films ($x \lesssim 1.33$), whereas reducing the N/Si ratio facilitates in the formation of Si−Si bonds. These silicon-rich films span a continuous compositional range, with $0.4 < x \leqslant 1.33$ being reported [152, 153]. The film density decreases with increasing Si content, ranging from $3.0\,\text{g}\,\text{cm}^{-3}$ for stoichiometric a-Si_3N_4 to $2.4\,\text{g}\,\text{cm}^{-3}$ for a-$SiN_{0.7}$, approaching the density of elemental silicon ($2.1\,\text{g}\,\text{cm}^{-3}$ [154]). Accordingly, higher Si fractions lead to a gradual reduction of the band gap from around 4.6 eV in the stoichiometric case down to ≈2.0 eV at $x = 0.5$ [155–157], eventually approaching 1.5 eV for a-Si:H [158]).

Furthermore, hydrogen incorporation is unavoidable (except for H-free sputtering) and elevated hydrogen concentrations lead to a reduced film density and lower mechanical strength as it interrupts the network connectivity [159, 160]. This is especially prevalent for plasma enhanced methods (PE-CVD and PE-ALD), which yield films containing between 5% and 20% hydrogen with densities between $2.0\,\text{g}\,\text{cm}^{-3}$ and $3.0\,\text{g}\,\text{cm}^{-3}$ [142, 151, 161–163]. A substantial fraction of hydrogen can be removed by post-deposition annealing at 800 °C to 900 °C [164], although residual hydrogen is often retained. During annealing, the thermally less stable Si−H bonds dissociate preferentially, forming either Si−Si bonds ($2\text{SiH} \rightarrow \text{Si} - \text{Si} + \text{H}_2$) or creating a defect. This leaves predominantly N−H configurations, while the film undergoes densification and surface smoothing. The role of hydrogen in the context of memory devices remains ambiguous. Hydrogen passivation is known to change the trapping characteristics, presumably due to passivating defects and thus their associated electronic states [52]. However, passivation and annealing affect multiple properties at once and the fact that charge trapping still occurs post passivation hints towards a more complex interplay between H incorporation, structural modification and charge trapping. Given the wide range of process parameters, it is therefore crucial to understand charge trapping processes on the atomic scale in order to predict the material behavior and to optimize the device performance.

3.2.2. The microscopic structure of a-SiN_x

The microscopic structure of a-SiN_x has primarily been investigated using x-ray and neutron scattering techniques. As is characteristic of amorphous solids, the pair correlation function $g(r)$ approaches unity at interatomic distances $r \gtrsim 6\,\text{Å}$, indicating the absence of long-range order [61]. In contrast, pronounced short-range order is evident from distinct features in $g(r)$ at smaller distances (figures 2(a) and (b)). The first sharp peak in $g(r)$ corresponds to the nearest-neighbor shell and is located at $r \approx 1.75\,\text{Å}$, which is in good agreement with the Si−N bond length in crystalline β-Si_3N_4. The second nearest-neighbor peak appears at approximately 3.05 Å, consistent with the Si−Si distance inferred from an average Si−N−Si

bond angle of about 120°. Similarly, assuming a tetrahedral N−Si−N bond angle of 109.47°, the corresponding N−N pair distance of 2.84 Å is observed in neutron scattering experiments [165]. In the presence of Si−Si bonds, for example in silicon-rich silicon nitride, a peak appears at the corresponding pair distance of 2.35 Å [49, 58].

Quantitative analysis of the first coordination shell shows a relatively narrow bond-length distribution, though the distribution has a long tail approaching 2 Å indicating the presence of highly stretched bonds. Fitting a Gaussian function to the first-neighbor peak yields a root-mean-square displacement of $\Delta r_{\mathrm{SiN}} = 0.071$ Å [165]. The second nearest-neighbor peaks exhibit broader distributions ($\Delta r_{\mathrm{SiSi/NN}} = 0.16$ Å), as the variations in bond lengths and angles progressively increase the disorder at medium ranges. Structural correlations beyond the second coordination shell are not discernible, indicating a complete loss of positional order at larger length scales due to the absence of constraints on Si−N−Si−N dihedral angles in the amorphous network [166].

Experimental evidence suggests that similar to β-Si_3N_4, the amorphous phase is comprised of corner-linked SiN_4-tetrahedra, but with the difference that their relative orientation is random such that they do not exhibit any long-range order (figure 2(c)). Accordingly, it has been suggested that a-Si_3N_4 can be reasonably well described as a *continuous random network* (CRN) [167]. The CRN model is defined as a three-dimensional, interconnected network of randomly oriented coordination polyhedra with all atoms being fully coordinated in accordance with their coordination shells being isostructural to their crystalline counterparts. Importantly, the CRN allows to systematically define 'defects' in the context of amorphous solids, such that vacancies correspond to missing nodes in the network, substitutions are nodal atoms that are replaced by another element, and interstitials are atoms that are placed in local cavities within the network.

In practice, even smooth a-$SiN_{x\approx1.33}$ films grown by LP-CVD deviate measurably from the ideal CRN. Integration of the nearest-neighbor peak of $g(r)$ yields average coordination numbers between 3.63 and 3.87 for silicon and between 2.72 and 2.91 for nitrogen, respectively [61, 165]. Hence, the coordination numbers deviate from the ideal coordination of 4 for silicon and 3 for nitrogen in crystalline Si_3N_4. Accordingly, the mass density is found to vary ranging from approximately 3.0 g cm^{-3} to 2.6 g cm^{-3} [99], suggesting the presence of microvoids and internal surfaces within the amorphous network. It is conceivable that a significant fraction of the apparent undercoordination arises from residual, network-terminating hydrogen, which is consistent with the broader range of densities and hydrogen concentrations observed in films grown using plasma-enhanced techniques. However, electron paramagnetic resonance (EPR) and photolumesence (PL) measurements reveal unpaired spin states that are associated with dangling Si and N bonds, which are commonly referred to as *K*- and *N*-centers, respectively [168–172]. Importantly, such EPR-active sites persist even in hydrogenated films, despite hydrogen being considered a passivation agent for dangling bonds.

In non-stoichiometric a-SiN_x, nitrogen deficiency is partially compensated by the formation of Si−Si bonds, such that the primary local bonding motifs are mixed tetrahedra of the form $Si(N_{4-x}Si_x)$ with $x \in [0, 4]$. These configurations are stable at room temperature; however, laser or thermal annealing above 1000 °C can induce phase separation, resulting in the formation of amorphous or crystalline silicon nanoparticles embedded within an amorphous silicon nitride matrix [173, 174].

4. Atomistic modeling of a-SiN_x

Understanding the origin of charge trapping processes in amorphous materials requires reliable models of the local atomic environments and its topological disorder. As defect properties are fundamentally linked to the local bonding configurations, it is crucial to generate computational models that accurately capture the structural features of a-Si_3N_4 thin films. Generating such models is challenging due to the inherently disordered atomic structure; therefore, we briefly review state-of-the-art modeling techniques.

4.1. Generating amorphous structures

Computational models of amorphous silicon nitride are most commonly generated by mimicking the vitrification process of a glass by melt-quenching (MQ) the system using molecular dynamics (MD) simulations [175–178]. In this approach, an initially crystalline supercell is heated above its melting temperature and equilibrated until all structural correlations associated with the starting configuration are lost. Loss of memory of the initial state can be verified, for example, by monitoring the decay of the positional autocorrelation function or by ensuring via the mean square displacement that atoms have diffused beyond a certain threshold, e.g. beyond the length of the simulation box. Subsequently, the system is cooled to room temperature at a well-defined quenching rate ($\mathrm{d}T/\mathrm{d}t$), typically on the order of

$10^{1}\,\mathrm{K\,ps^{-1}}$ down to $10^{-2}\,\mathrm{K\,ps^{-1}}$. The quench is usually performed under either constant-volume (*NVT*) or constant-pressure (*NpT*) conditions, with the latter being generally preferred, as it allows the simulation cell to relax freely and reduces the risk of forcing the system into artificially strained or high-pressure configurations during the glass transition. Finally, the amorphous structure is equilibrated at room temperature, after which structural, vibrational, or electronic properties can be evaluated using first-principles calculations.

This approach implicitly assumes that the short-range structure of the amorphous solid evolves continuously from that of the corresponding liquid, since the melt-quench MD procedure necessarily involves a continuous glass transition without discontinuities in density or local coordination [179]. As a result, amorphous materials whose structure is strongly shaped by non-equilibrium growth mechanisms, such as ion bombardment, sol-gel processing, or CVD, typically cannot be reproduced quantitatively by MQ simulations. In the specific case of *a*-Si_3N_4, however, SiN_4 tetrahedra dominate both MQ-MD generated structures and the films deposited from the gas phase, justifying this approach to be representative. The structural fingerprints obtained from MQ-MD models, including pair correlation functions and density, are in good agreement with the experimental data discussed in section 3.2.2, see figure 2. However, features like $g(r)$ or the density average over hundreds or thousands of atoms and therefore may mask nonphysical outliers. Therefore, it is crucial to also benchmark local features like coordination numbers and symmetry and derived quantities like vibrational spectra, bulk modulus, etc to validate the model. Given that these requirements are met, three-dimensional bulk melt-quench structures are assumed to provide a reasonable representation of dense amorphous *a*-Si_3N_4 films grown under thermal conditions and exhibiting low to moderate defect concentrations.

When applying a MQ-MD protocol, it is essential to carefully benchmark the simulation settings, as amorphous systems are particularly sensitive to finite-size effects arising from the use of periodic boundary conditions. Periodic boundary conditions are required to represent bulk behavior, but they also impose an artificial translational periodicity that is absent in a truly amorphous solid. As a result, the simulation cell must be sufficiently large to prevent spurious self-correlation across periodic images. In practice, this requires the size of the simulation box to exceed the characteristic length scale of structural correlations, e.g., at least twice the distance at which the pair correlation function approaches unity.

Similarly, the time scale of the quenching process has a major impact on the resulting amorphous structure. Cooling rates typically employed in MQ-MD simulations still exceed those achievable in experimental vitrification by many orders of magnitude, where effective cooling rates are on the order of 10^{-10} $\mathrm{K\,ps^{-1}}$ to 10^{-12} $\mathrm{K\,ps^{-1}}$ [180]. As a consequence, the simulated system can persist in metastable, relatively high-energy configurations, as the structure does not have sufficient time to relax during the glass transition [181]. MQ-MD structures therefore have larger positive formation energies compared to real samples [182, 183] (referenced against the crystalline phase). This incomplete structural relaxation leads to a broadening of both global and local structural distributions of observables across an ensemble of independently generated amorphous models, including density, bond lengths, and bond angles [184]. Critically for charge-trapping studies, this also affects the concentration of over- and undercoordinated atoms [185]. While this limitation cannot be fully eliminated, careful benchmarking of the simulation cell size and cooling rate allows the modeling protocol to be tuned such that key structural observables fall within the experimentally observed range.

These considerations also affect the choice of the interatomic interaction model. First-principles methods such as DFT are, in principle, applicable [50]; however, the computational cost associated with evaluating forces at each MD step severely constrains their use to small simulation cells and very rapid quench rates. This limitation often results in unphysically high concentrations of coordination defects and other artifacts in melt-quench simulations. For this reason, classical interatomic potentials have been widely employed to generate amorphous silicon nitride structures, as they enable MD simulations with larger system sizes and longer trajectories, thereby mitigating many of the finite-size and quench-rate related artifacts discussed above. For *a*-Si_3N_4, several classical potentials have been developed, including parameterizations based on the Tersoff [186–188], Vashishta [189], Stillinger-Weber [190], and Morse formalisms [191]. A comprehensive benchmark comparing these interaction models is provided in [192]. Because amorphous structures are intrinsically metastable and their structural observables are distributed over finite ranges, the reduced accuracy of classical potentials plays a relatively minor role, provided that the average pair interactions are described reasonably well. The main limitation of classical interatomic potentials, however, is their restricted transferability: they are typically parameterized for monoatomic or binary systems and lack the flexibility required to accurately capture a wide variety of local bonding environments. This limitation may be alleviated by the rapid development of machine-learned interatomic potentials, with several recent studies highlighting their potential to combine near first-principles accuracy with the efficiency required for large-scale amorphous simulations [193–197].

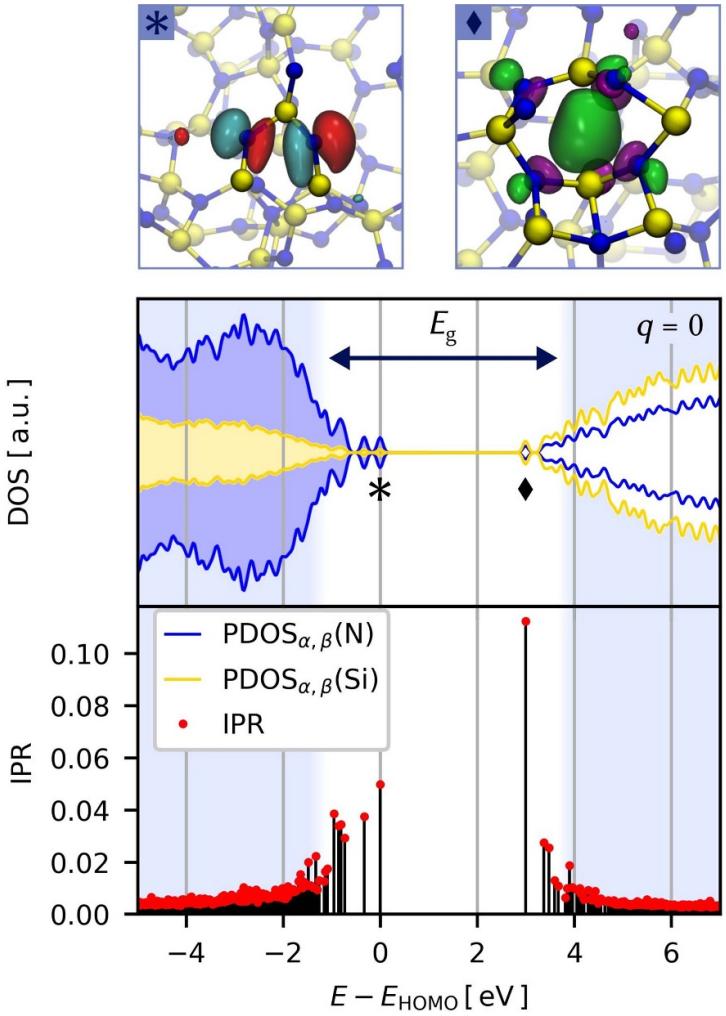

Figure 3. Upper panel: Illustration of the highest occupied/lowest unoccupied Kohn–Sham state above the VBM/below the CBM, respectively. Middle panel: The projected electronic density of states (PDOS) of nitrogen (blue) and silicon (yellow) relative to the HOMO (E_{HOMO}) in a neutral, 280 atoms supercell. Lower panel: The inverse participation ratio (IPR) of the associated eigenstates. The shaded energy ranges mark the delocalized valence and conduction band states, with the boundary between localized and delocalized states being considered the mobility edge. All data is obtained from DFT calculations at the HSE06 level. Reproduced from [53] CC BY 4.0.

4.2. The electronic structure of *a*-Si_3N_4

The calculated band gap of *a*-Si_3N_4 typically lies between 3.5 eV and 5.0 eV [53, 65], which is in good agreement with the experimentally reported range of 4.2 eV to 5.4 eV [107, 156, 198]. Closer inspection of the band edges reveals that both the valence band maximum (VBM) and the conduction band minimum (CBM) are dominated by localized Anderson states. The VBM has predominantly N-character, whereas the CBM is primarily composed of Si-dominated states [46, 47, 53]. These states are referred to as *N*- and *K*-centers, respectively.

The electronic ground state of these models is typically low-spin, such that the edge states are either fully occupied or unoccupied, consistent with the negative-*U* behavior of dangling-bond centers, i.e., *N* and *K*-centers undergo donor–acceptor compensation via $N^0 + K^0 \rightarrow N^- + K^+$ leading to a low-spin ground state configuration [172]. A representative example of the electronic density of states (DOS) is shown in figure 3. The localized states near the band edges are associated with structurally distorted nitrogen and silicon sites, ranging from moderately deformed coordination polyhedra to fully broken bonds resulting in undercoordinated atoms. Owing to the amorphous nature of the network, the transition from a distorted to a truly defective coordination environment is continuous: the bond-length distribution exhibits a long tail (figure 2(a)), such that a threshold solely based on pair distance to distinguish an elongated bond from a broken one does not exist. More in-depth electronic structure analysis using maximally-localized Wannier functions [199] has shown that Si−N pairs approaching 2.0 Å can still be covalently bonded [46, 52] and can play an important role for the reversible capture of charge carriers in *a*-Si_3N_4 (section 6.2). In addition, a correlation between the degree of angular opening of a

coordination polyhedron and the presence of localized states has been reported [53], with more open sites coinciding with stronger localization. However, the ubiquity of such deformed polyhedra prevents predicting electron localization solely based on geometric criteria.

Employing first-principles calculations, the degree of localization of an electronic state i in a system of N atoms can be quantified from the coefficients of the associated wave function in an atom-centered (Gaussian) basis set using the *inverse participation ratio* (IPR), defined as

$$\mathrm{IPR}\,(i) = \frac{\sum_j^N c_{ij}^4}{\left(\sum_j^N c_{ij}^2\right)^2}\ , \tag{1}$$

where c denotes the coefficients of the wave function of state i projected onto the basis functions of atom j. In the fully localized limit, where the wave function is confined to a single atom, the IPR approaches 1, whereas in the completely delocalized case it approaches $1/N$, with N being the number of atoms in the supercell. As illustrated in the lower panel of figure 3, states deep inside the valence and conduction bands exhibit low IPR values, consistent with their extended, delocalized character in a periodic supercell representation. In contrast, states near the band edges show progressively larger IPR values, reflecting increased localization. The strongest localization is typically observed for states located deepest within the band gap [47].

As the band edges are dominated by defective localized states, their frequency and relative energy level vary from cell to cell as they arise from different defect configurations, which are further influenced by the varying chemical environment. Consequently, the highest occupied states reside on different defective nitrogen sites in different configurations. Strictly speaking, this renders the highest occupied molecular orbital (HOMO) level non-transferable between individual supercells, as it is determined by configuration-specific localized states rather than by an extended band edge. The same considerations apply for the lowest unoccupied molecular orbitals (LUMO) centered on Si atoms.

Moreover, strongly localized states near the band edges are not fully compatible with the conventional band picture of crystalline solids, which assumes well-defined, extended Bloch states. A more coherent description is therefore obtained by interpreting these states as part of an Urbach-like tail [200] extending from the band edges into the gap. Within this framework, the HOMO and LUMO determined from computational models should not be considered as the VBM and CBM, respectively. Instead, the mobility edge [201] can be defined using an IPR threshold that distinguishes extended from localized states [176]. An unambiguous numerical value for this threshold cannot be specified, since the decay of the IPR is continuous and the energy range of localized and delocalized states overlap (see figure 3, lower panel). Nevertheless, referencing against the mobility edge of the valence or conduction band allows to systematically compare ensembles of supercells and establishes a rigorous basis for discussing amorphous silicon nitride within the context of semiconductor physics.

It must be noted that the distinction between localized and delocalized states based on the IPR is only possible in a theoretical framework. While first-principles calculations provide strong evidence for this model, direct experimental observation of (semi-)localized states is only feasible at ultra-cold temperatures, e.g. by spatially probing the states using scanning tunneling spectroscopy or by characterizing the Urbach tail via optical absorption measurements [202–204]. Thus, localized states in the a-Si_3N_4 layer of CTF can only be probed indirectly by comparing predictions with observations in real devices.

Structures generated by classical interaction potentials [46, 53, 205], machine learning interaction potentials [51, 52, 65, 193], or *ab initio* MD [49, 50, 55–57] are equally suitable for follow-up DFT calculations to obtain deeper insights into the electronic structure, provided that artifacts arising from finite-size effects and quench-rate limitations are sufficiently controlled. When analyzing the electronic structure, however, the choice of exchange-correlation functional becomes critical, since not all functionals describe defect-related states with sufficient accuracy. In particular, generalized gradient approximation (GGA) functionals are well known to underestimate the band gap and often fail to accurately describe the localization of electronic states, which is crucial to study charge transitions at defect sites [117, 206]. As a result, moderately localized defect states near the band edges may be artificially smeared out, which compromises the determination of the mobility edge and the associated challenges described above. This issue is especially problematic here, where the transition between extended band states and localized tail states is gradual rather than sharply defined (see figure 3, lower panel).

For these reasons, hybrid exchange-correlation functionals, which incorporate a fraction of exact Hartree–Fock exchange, are typically required to obtain a quantitatively reliable description of defect states and band-tail localization in amorphous silicon nitride. By partially alleviating the self-interaction

error inherent to semi-local functionals, hybrid approaches improve the localization behavior and energetic placement of charged defect states. The percentage of exact exchange can be fitted to, for example, the experimentally determined band gap. This, however, would require a clear fitting target, which is not necessarily given for a-SiN_x due to the variety of process conditions and material properties (see section 3). In practice, well-benchmarked defaults, e.g. 25% for HSE06 or PBE0 [207–211], are considered to be sufficiently accurate given that instead of yielding a singular number, observables measured for amorphous systems are inherently distributed over a particular range.

5. Fundamentals of charge trapping

The unoccupied localized states close to the conduction band introduced by structural defects are suitable precursors for trapping excess electrons from the Si substrate of a CTF device. When the localized electronic state becomes occupied by an electron, the attractive and repulsive forces at the defect site change, leading to structural relaxations of the atomic structure to a different minimum energy configuration in the negative charge state. In recent years, methodologies have been developed to analyze charge transitions at point defects using first-principles calculations [68, 69, 212], which we will summarize in the following. In particular, we will outline the NMP charge capture process of trapping electrons from the mobility edge of a-Si_3N_4 at intrinsic defect sites. The structural features of these defects and their charge trapping properties within the NMP model will then be discussed in section 6.

5.1. Nonradiative multiphonon charge transitions

The interaction of charge carriers with the atomic structure necessitates the inclusion of electron–phonon coupling effects when describing charge trapping at defect sites to capture the structural reconfigurations [213, 214]. For the remainder of this paper, we will use the notation q_1/q_2 to indicate a transition of a defect from charge state q_1 to q_2, e.g. $q_1 = 0$ and $q_2 = -1$ for electron capture. The charge transition rate $k_{0/-1}$ caused by a perturbation $\hat{H}'$ between the two defect charge states 0 and -1 is given by Fermi's golden rule

$$k_{0/-1} = \frac{2\pi}{\hbar} \left| \langle \Psi_0 | \hat{H}' | \Psi_{-1} \rangle \right|^2 \delta \left(E_{-1} - E_0 \right). \tag{2}$$

Here, $\Psi_{0,-1}$ are the total wave functions of the initial and final states with energy $E_{0,-1}$. The Dirac-delta ensures energy conservation between the initial and final state.

To analyze the electron capture processes in a-Si_3N_4 with DFT using equation (2), it is necessary to apply additional approximations, which have been assessed in [69] and are adopted for the calculations in this work. Following the Born-Oppenheimer approximation, the wave function of the defect system Ψ_i can be written as a product of an electronic wave function ψ_i and a vibrational wave function χ_i. This allows for the description of the atomic trapping site in the neutral and negative charge state by two distinct potential energy surfaces.

Additionally, we employ the static coupling approximation, evaluating the electronic wave functions at a fixed atomic configuration Q_0 [215, 216]. We also assume linear electron–phonon coupling by Taylor-expanding the matrix element up to first order around Q_0, which was chosen as the equilibrium geometry of the neutral defect state. This geometry is considered as an appropriate choice, since the defect states in Q_0 are well defined in the band gap, and thus yield suitable bulk and defect wave functions for perturbation theory [69]. Finally, we will reduce the vibrational degrees of freedom to a single effective phonon mode. The resulting one-dimensional (1D) potential energy curve (PEC) has been proven to efficiently capture the structural relaxations of deep traps with strong electron–phonon coupling [68]. In particular for defects with Huang–Rhys factors $S \gg 1$, the 1D approximation accurately reproduces the displacement and energy scaling of the entire phonon mode spectrum [217]. This justifies its application to intrinsic electron traps in a-Si_3N_4, where relaxation energies are on the order of 1 eV and above [51, 52, 65].

5.1.1. Configuration coordinate diagram for electron capture in a-Si_3N_4

The effective-phonon mode approximation allows for the treatment of the charge transition in an one-dimensional configuration coordinate diagram (CCD). Here, we discuss the nonradiative capture of an electron at an intrinsic acceptor site from a conduction band state in a-Si_3N_4 and exemplarily construct the CCD for such a process. In this framework, we assume that the electron, which can be for example injected from the Si substrate of an CTF as discussed in section 2, initially occupies a delocalized state at the mobility edge (see 4.2) before transitioning to a localized defect state. This process is analogous

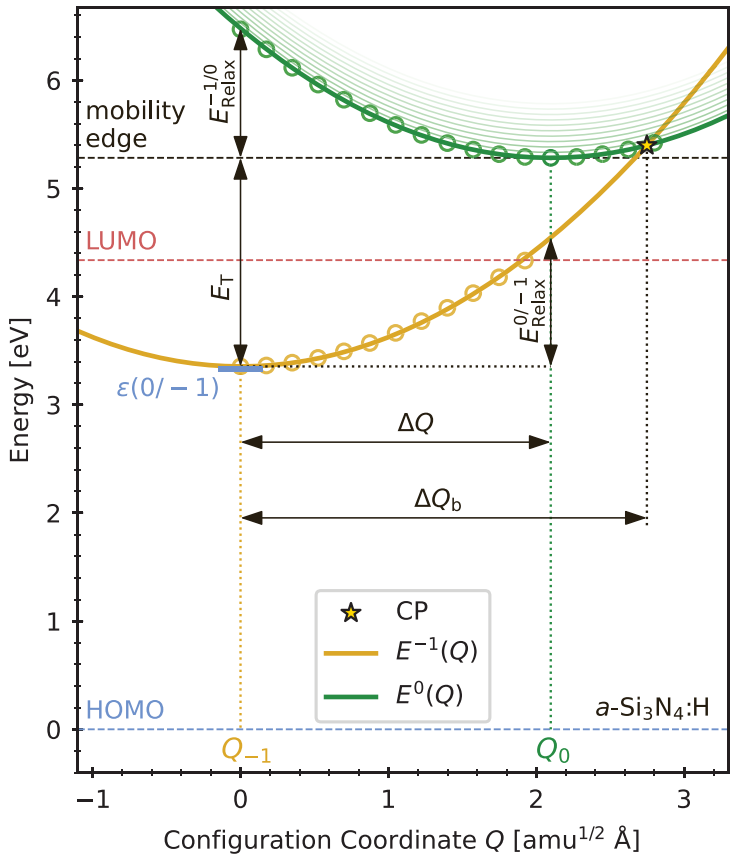

Figure 4. One-dimensional configuration coordinate diagram (CCD) for the nonradiative capture of an electron from the mobility edge of a-Si_3N_4 at an intrinsic electron trap in a-Si_3N_4. The CCD for this transition is defined by the electronic band gap, the charge-state transition level $\varepsilon(0/-1)$, the configuration coordinate change ΔQ, and the total energies as a function of Q in both charge states, including the relaxation energies $E_{\mathrm{Relax}}^{q_1/q_2}$. The thermodynamic trap level E_{T} is defined as the energy difference of the defect system in charge states $q = 0$ and $q = -1$, evaluated at their respective minimum energy configurations Q_0 and Q_{-1}. The classical energy barrier for electron capture $E_{\mathrm{b}}^{0/-1}$ is given by the energy difference from the mobility edge to the crossing point, and vice versa $E_{\mathrm{b}}^{-1/0}$ for electron release from $\varepsilon(0/-1)$ to the crossing point. The PECs to evaluate electron capture for initial delocalized states higher in the conduction band are schematically drawn as thin green lines above $E^0(Q)$. Data obtained from postprocessing of calculations presented in [52].

to electron capture at an acceptor defect from a delocalized bulk state in crystalline semiconductors, for which the theory of NMP transitions was originally developed. We note that the same methodology can be applied for electrons initially occupying higher states in the conduction band prior to the localization, which will be further discussed in section 6.4.

The CCD for the capture of an electron from the mobility edge of a-Si_3N_4 at an intrinsic defect site in a-Si_3N_4 is illustrated in figure 4. The yellow and green parabolas represent the PECs of the trapping site in the negative (with a localized electron) and neutral (electron in the conduction band) charge states. These PECs can be obtained by parabolic fits to the total energies of linearly interpolated images between the minimum energy configurations in both charge states, Q_0 and Q_{-1}. The total configuration coordinate change is given by ΔQ, $\varepsilon(0/-1)$ is the thermodynamic charge-state transition level (CTL) of the intrinsic defect, while $E_{\mathrm{Relax}}^{0/-1}$ and $E_{\mathrm{Relax}}^{-1/0}$ are the relaxation energies of the transition, and ΔQ_{b} is the configuration coordinate change to the crossing point. The HOMO, LUMO and the mobility edge of a-Si_3N_4 are shown as dashed lines. All depicted properties can be evaluated with first-principle methods as will be discussed in section 5.3.

We note that in principle the transition of a charge carrier from a band to a defect site and vice versa can be either radiative or nonradiative. Following the Franck-Condon principle [214], the radiative charge transfer corresponds to a vertical transition in the CCD, where the energy difference between unoccupied and occupied state is released via light emission (photons). For the nonradiative transition, the energy is released to the surrounding lattice via multiple phonons, hence the name NMP transition. Since optical excitations are typically not observed in CTF devices, we asses the probability of charge transitions at a defect site in a-Si_3N_4 within the NMP framework.

5.2. Charge capture coefficient from first-principles

In this section we will outline the methodology to analyze the electron trapping probability of a defect site by evaluating the charge capture coefficient of an intrinsic electron trap in a-Si_3N_4 at room temperature. We will further describe how to obtain the defect parameters needed to construct the CCD in figure 4 with DFT.

Charge transition rate

The charge transition rate given in equation (2) accounts for the capture rate of a single electron at a single defect site. The full nonradiative electron capture rate in a system with electron density n_e and a concentration of acceptor-like defects N_A can be written as a function of the temperature T with [218]

$$R_{0/-1}(T) = C_{0/-1}(T) N_\mathrm{A} n_\mathrm{e}, \tag{3}$$

where $C_{0/-1}(T)$ is the T-dependent capture coefficient of one electron at one defect within a simulated supercell with volume V. $C_{0/-1}$ is related to the charge transition rate in equation (2) by $C_{0/-1} = Vk_{0/-1}$ and can be directly evaluated with first-principles methods such as DFT [69].

By employing the approximations summarized in section 5.1, $C_{0/-1}$ is given by

$$C_{0/-1}(T) = Vk_{0/-1} = \frac{2\pi}{\hbar} V |\theta_{0/-1}(Q_0)|^2 \xi_{0/-1}(T), \tag{4}$$

where $\theta_{0/-1}(Q_0)$ is the electron–phonon coupling element, evaluated at the minimum energy configuration of the neutral charge state Q_0, and $\xi_{0/-1}(T)$ is the line shape function depending on the temperature T and is related to the thermally averaged overlap of the vibrational wave functions of both states. In general, if a defect is already charged prior to the transition, the Sommerfeld parameter must also be included as a linear factor to account for the disturbance of the conduction band wavefunction by the localized defect charge [219]. For the present work, the inclusion of the Sommerfeld parameter is not necessary, since we are primarily interested in the capture process of an electron at a previously neutral defect.

5.2.2. Classical charge transition barriers

The electron capture from the mobility edge can be intuitively understood in the classical picture when looking at the CCD in figure 4. In equilibrium, the system is at the minimum of the respective PEC, which is located at a state in the conduction band, specifically shown here as the mobility edge. If sufficient thermal energy is supplied to the defect site, e.g. in the form of multiple phonons, the system is elevated up to the energy of the crossing point (E_CP), where the defect can capture an electron and relax to the new minimum energy configuration in the negative charge state. The classical barrier $E_\mathrm{b}^{0/-1}$ for electron capture from a state at the mobility edge at a trapping site in a-Si_3N_4 is given by the energy difference between the crossing point of the two PECs and the respective initial state ϵ_i

$$E_\mathrm{b}^{0/-1} = E_\mathrm{CP} - \epsilon_i. \tag{5}$$

Vice versa, for electron emission from the defect to the mobility edge, the barrier $E_\mathrm{b}^{-1/0}$ is given by the energy difference between the charge state-transition level of the trapping site $\varepsilon(0/-1)$ and the crossing point.

$$E_\mathrm{b}^{-1/0} = E_\mathrm{CP} - \varepsilon(0/-1). \tag{6}$$

5.2.3. Line shape function at room temperature

For defects transitions with sufficiently large structural relaxations, $\xi_{0/-1}(T)$ in equation (4) can be captured by a classical model for the line shape function in the limit of high temperatures (T∼293 K and above) [70, 72, 220]

$$\xi_{0/-1}(T) = \xi^0_{0/-1}(T) f_{0/-1}(T) = \xi^0_{0/-1}(T) \exp\left\{\left(-\frac{E_\mathrm{b}^{0/-1}}{k_\mathrm{B}T}\right)\right\}, \tag{7}$$

where $f_{0/-1}(T)$ is an Arrhenius-like factor depending on $E_\mathrm{b}^{0/-1}$ and $\xi^0_{0/-1}(T)$ is a prefactor depending on the shape of the PECs of the defect in charge state 0 and −1, given by [70, 73, 221]

$$\xi^0_{0/-1}(T) = \sqrt{\frac{E_\mathrm{Relax}^{-1/0}}{4\pi k_\mathrm{B} T}} \frac{|\Delta Q|(\Delta Q_\mathrm{b})^2}{\left|\left(E_\mathrm{Relax}^{-1/0} - E_\mathrm{Relax}^{0/-1}\right)(\Delta Q_\mathrm{b} - \Delta Q) + E_\mathrm{Relax}^{0/-1}\Delta Q\right|}. \tag{8}$$

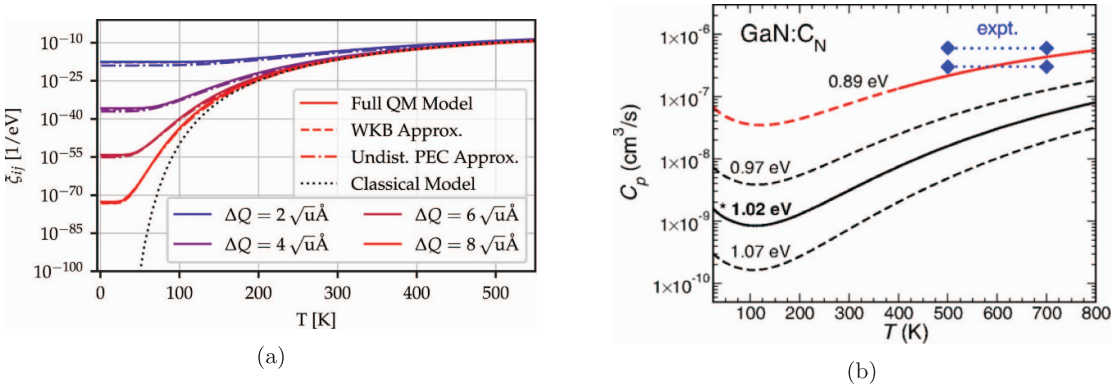

Figure 5. (a) Lineshape function ξ_{ij}, $i = q_1$ and $j = q_2$, of an exemplary defect for varying configuration coordinate changes ΔQ calculated with different models, including the full quantum mechanical model and the classical approximation as discussed in the main text. Reproduced from [72]. CC BY 4.0. (b) Calculated nonradiative hole capture coefficient of the C_N defect in GaN as a function of temperature for varying energy offsets between the two parabolas. Reprinted (figure) with permission from [69], Copyright (2014) by the American Physical Society.

The validity of the classical approximation is demonstrated in figure 5(a), where the line shape function of an exemplarily defect was calculated for varying ΔQ in the full quantum mechanical treatment and with different approximations [72]. At 300 K and above, the classical model agrees well with the full quantum-mechanical description, in particular for charge transitions with configurational changes $\Delta Q > 2\sqrt{\mathrm{u}}$Å.

We note that at cryogenic temperatures, the error introduced by the classical approximation can be several orders of magnitude. This is because the charge transition at cryogenic temperatures can also occur below the crossing point due to quantum mechanical tunneling, and charge transition rates are thus considerably underestimated in the classical model [69, 70, 72, 220]. In this case, the vibrational wavefunctions of the PECs have to be explicitly obtained and their thermally averaged overlap has to be calculated to capture the full transition probability. However, for analyzing charge trapping in CTF devices, which are typically operated at room temperature, the classical treatment is considered sufficient for the present discussion.

5.2.4. Electronic matrix element

Following perturbation theory, the electronic-phonon matrix element can be expressed as [222]

$$\theta_{0/-1}(Q_0) = (\varepsilon_f - \varepsilon_i)\left\langle \psi_i \middle| \frac{\partial \psi_f}{\partial Q} \right\rangle, \tag{9}$$

with $\varepsilon_{i,f}$ and $\psi_{i,f}$ being the energies and single-particle wave functions of the initial and final electronic states, respectively. For the process considered in this work, ψ_i corresponds to a delocalized state at the mobility edge, and ψ_f is the localized state at the intrinsic defect. The matrix element is hereby evaluated at the minimum energy configuration of the neutral charge state Q_0 [69]. Since the mobility edge is not well defined in a-Si_3N_4 but distributed, $\theta_{0/-1}(Q_0)$ can slightly change depending on the specific initial state ψ_i considered for the transition. However, we find that the inaccuracies of varying electron–phonon matrix elements between different conduction band states in the prefactor $\theta_{0/-1}$ are comparably small. From equations (4) and (7), it is clear that $E_b^{0/-1}$ has the largest impact on the charge transition rate of all defect-related variables, as it enters the equation in the exponential factor $f_{0/-1}(T)$. Therefore, varying the thermal barrier by 0.1 eV (0.2 eV) already changes $f_{0/-1}(T)$ by almost two (four) orders of magnitude at room temperature where the thermal energy k_BT is ∼25 meV. The overpowering impact of the thermal barrier has also been explicitly shown for the hole capture coefficient C_p of the C_N defect in GaN in figure 5(b) [69], where C_p is evaluated as a function of temperature for varying barriers between the two parabolas in the CCD. These calculations demonstrate that small deviations of the barrier by 50 meV can change the capture coefficient by almost one order of magnitude. Since such small inaccuracies in energies are well within the error range of DFT for defect calculations, only the order of magnitude of $C_{0/-1}$ can be reasonably estimated within the employed methodology. The impact of the initial state on electron trapping in a-Si_3N_4 will be further discussed in section 6.4.

5.2.5. Capture cross section at room temperature

Equation (4) provides a fully quantum-mechanical description of the charge capture coefficient. In semiconductor device engineering, the charge transition rates at defects are often approximated by the Shockley–Read–Hall (SRH) model, which provides a phenomenological interpretation of the trapping dynamics.

The capture coefficient in the SRH model is commonly given as a product of the thermal velocity $\nu_{\mathrm{th}} = \sqrt{8k_{\mathrm{B}}T/\pi m^*}$ and a phenomenological capture cross section $\sigma^{\mathrm{SRH}}_{0/-1}$, with m^* being the effective mass of the electron ($m^* \approx 0.5\,\mathrm{m}_0$ for a-Si_3N_4 [223]).

$$R^{\mathrm{SRH}}_{0/-1} = \sigma^{\mathrm{SRH}}_{0/-1} \nu_{\mathrm{th}} N_{\mathrm{A}} n_{\mathrm{e}}. \tag{10}$$

To relate the phenomenological SRH model against the quantum-mechanical NMP theory, a capture cross section can also be defined in NMP [69] by comparing equation (3) with equation (10), yielding

$$\sigma_{0/-1}(T) = \frac{C_{0/-1}(T)}{\nu_{\mathrm{th}}(T)} = \frac{2\pi}{\hbar}\frac{1}{\nu_{\mathrm{th}}(T)} V \left| \left(\epsilon_f - \epsilon_i\right) \left\langle \psi_i \middle| \frac{\partial \psi_f}{\partial Q} \right\rangle \right|^2 \xi^0_{0/-1}(T) \exp\left(-\frac{E_{\mathrm{b}}^{0/-1}}{k_{\mathrm{B}}T}\right). \tag{11}$$

Equation (11) will be used to evaluate the electron capture cross sections of intrinsic electron traps in section 6.4.

Because SRH neglects electron–phonon coupling effects during the charge transfer, it is generally not suited to account for the activation barrier of the charge capture process and to describe the structural relaxations induced by charge trapping [71]. However, for electron trapping at intrinsic defects in a-Si_3N_4, we find that the activation barrier is only in the range of a few phonon quanta (see figure 4), and temperature-mediated effects for this process are expected to be comparably small. Consequently, SRH models can provide a reasonable approximation of the charge transfer at room temperature, particularly because some temperature dependence is already accounted for via the thermal velocity of the charge carriers, while the capture cross-section itself is treated as a constant. In contrast, $\sigma_{0/-1}(T)$ evaluated with NMP explicitly accounts for the temperature dependence of the charge transition rate, a behavior that has been well-documented in experiment [224–226].

5.3. Electron trap characterization – modeling the PECs

Following the effective phonon mode approximation discussed above, only the configuration coordinate change ΔQ, the CTL $\varepsilon(0/-1)$ and the relaxation energies $E^{q_1/q_2}_{\mathrm{Relax}}(Q)$ have to be calculated with DFT to model the PECs and to subsequently extract the classical transition barriers from the PECs. The methodology to evaluate these properties with DFT will be outlined in the following.

5.3.1. Thermodynamic charge-state transition level

The CTL of a trapping site gives the electronic level $\varepsilon(q_1/q_2)$ of the charge transition between charge state q_1 and q_2. In the CCD, the CTL defines the offset of the parabolas with respect to the charge reservoir, and consequently determines the classical energy barrier of the NMP transition.

The CTL can be obtained from formation energy evaluations of the trapping site. The formation energy E^q_{form} of an intrinsic defect in charge state q is given by [227]

$$E^q_{\mathrm{form}} = E^q_{\mathrm{tot}} - E^{\mathrm{bulk}}_{\mathrm{tot}} + \sum_i n_i \mu_i + q E_{\mathrm{F}} + E^{\mathrm{corr}}, \tag{12}$$

where E^q_{tot} is the total energy of a supercell containing the defect in charge state q, and $E^{\mathrm{bulk}}_{\mathrm{tot}}$ is the total energy of the pristine bulk supercell. n_i is the number of species i removed from or added to the system with the corresponding chemical potential μ_i. For the case of intrinsic trapping, this term does not need to be considered, since here $n_i = 0$. E_{F} is the Fermi energy referenced to the VBM of the pristine cell and E^{corr} is an *a posterio* correction term needed for DFT calculations of charged systems [228].

To analyze the stability of a trapping site in different charge states, E^q_{form} can be conveniently plotted in a formation energy diagram as a function of Fermi levels across the electronic band gap of the insulator. This is illustrated for an intrinsic electron trap in a-Si_3N_4 in figure 6 [52], where the HOMO and LUMO are drawn as vertical dashed lines. The CTL marks the energy level where E^q_{form} in two charge states are equal, indicating that the thermodynamically preferred charge state changes when crossing the CTL at

$$\varepsilon(0/-1) = \frac{E^0_{\mathrm{form}}(E_F = 0) - E^{-1}_{\mathrm{form}}(E_F = 0)}{-1 - 0}. \tag{13}$$

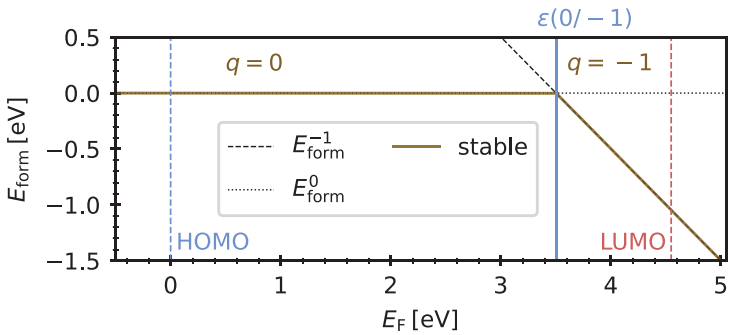

Figure 6. Formation energy diagram of an intrinsic electron trapping site in a-Si_3N_4. Energies of HOMO and LUMO are drawn as vertical dashed lines. The stable charge state with respect to the Fermi level is illustrated as a bold line.

For the example of a single electron trap this means that if the Fermi level is below $\varepsilon(0/-1)$, the defect has a lower formation energy when uncharged and is stable in the neutral charge state. For Fermi levels above $\varepsilon(0/-1)$, the defect has a lower formation energy in the negative charge state and is thus thermodynamically stable with a trapped electron.

In electronic device engineering, CTLs are commonly associated with the trap level E_T, which is given by the energy difference between CTL and charge reservoir. For electron trapping from a conduction band state ϵ_i, the trap level is accordingly given by $E_T = \varepsilon_i - \varepsilon(0/-1)$.

5.3.2. Configuration coordinate change

The configuration coordinate change ΔQ in equation (8) encodes the mass-weighted structural distortion of all atoms in the system upon charge transfer. It is given by

$$\Delta Q = \sqrt{\sum\nolimits_{\alpha,i} m_\alpha \Delta R^2_{\alpha,i}}, \tag{14}$$

where $\Delta R_{\alpha,i}$ is the displacement vector of atom α with atomic mass m_α along the three Cartesian coordinates $i = x,y,z$ and typically expressed in units $\sqrt{\text{amu}}$Å. The equilibrium configuration coordinates of the negative (gold) and neutral (green) charge states in figure 4 are given by Q_{-1} and Q_0, respectively, and can be obtained with DFT by geometry optimizations of a defect structure in different charge states.

5.3.3. Relaxation energy and effective phonon mode

The effective phonon modes of a charge transition can be constructed by calculating $E^q(Q)$ of linearly interpolated structures between the atomic coordinates Q_{-1} and Q_0. For the example shown in figure 4, the PECs of the transition correspond to a defect structure from [52], where $E^q(Q)$ were calculated with hybrid DFT. Typically, atoms near the localized charge contribute more to ΔQ, as they experience larger relaxations than atoms far from the trapping site. A parabolic function was fitted to the $E(Q)$ to analytically describe the harmonic PECs, as will be further discussed in section 6.4. The energy difference in charge state $q = -1$ between configuration Q_0 and Q_{-1} gives the relaxation energy

$$E^{0/-1}_{\text{Relax}} = E^{-1}(Q_0) - E^{-1}(Q_{-1}), \tag{15}$$

and vice versa

$$E^{-1/0}_{\text{Relax}} = E^{0}(Q_{-1}) - E^{0}(Q_0), \tag{16}$$

for the energy difference between configuration Q_{-1} and Q_0 in charge state $q = 0$.

6. Charge trapping mechanisms in silicon nitride

The first computational studies to understand charge trapping in silicon nitride used β-Si_3N_4 as a proxy for the amorphous phase due to the limitations in computational resources at the time [66, 123–127]. These studies identified that point defects play a central role by introducing localized electronic states within the band gap. While crystalline models establish the basic physics of these coordination defects, only amorphous models can represent the structural disorder inherent in a-Si_3N_4 thin films, which is crucial to capture the full complexity of the electron trapping processes.

6.1. Single defect levels in crystalline silicon nitride

Among the various defects studied in β-Si_3N_4, including interstitials, substitutional defects and vacancies, the dangling silicon bonds associated with nitrogen vacancies (V_N) are most prominently linked to the formation of localized gap states [123, 124, 126]. The precise level of these states varies depending on the modeling approach, i.e. atomic cluster vs. 3D periodic bulk, (partial) hydrogen termination of dangling bonds, and the formation of Si−Si bonds. The CTL lies typically between 1.4 eV to 2.0 eV below the conduction band (see table 2), and if the models include suitable states, they undergo the same donor–acceptor compensation as neutral a-Si_3N_4, see section 4.2. However, since the various V_N models yield similar CTLs, it remains difficult to identify a single, unique trapping mechanism based solely on electronic energies.

By calculating the hyperfine coupling constants of ^{29}Si in a three-dimensional periodic supercell containing a V_N defect, DiValentin *et al* [126] demonstrated that the best agreement with experimental EPR data is obtained when two three-coordinated silicon atoms $(N-)_3Si\cdot$ adjacent to the vacancy form a $N_3Si-SiN_3$ bond. This result supports the hypothesis that silicon-rich local environments are closely associated with electrically active defect centers [67].

Despite good agreement with experimental observations, these early crystalline models could not account for the structural disorder and extensive bond angle/length variation that are intrinsic to the amorphous phase, which can substantially influence defect formation energies, electronic states, and carrier localization. In a perfect β-Si_3N_4 lattice, an isolated point defect such as V_N produces a single mid-gap state [127], limiting the variety of accessible trap sites. In contrast, the amorphous network hosts a broad distribution of local environments and defect geometries, enabling multiple, distinct trap states [176]. Therefore, the amorphous phase must be modeled explicitly to obtain a holistic picture of charge trapping mechanisms in a-SiN_x.

6.2. Variety of electron trapping sites in amorphous silicon nitride

Based on EPR-studies by Lenahan *et al* [229–231] and others [232–234] in the early 1990s combined with theoretical considerations by Robertson *et al* [168–172], dangling silicon bonds ($N_3Si\cdot$) have been originally proposed as the origin of charge trapping in a-Si_3N_4. Due to the high computational demand required, it was only in the 2010s when Vedula *et al* [46, 48] and Hintzsche *et al* [47, 49] performed the first atomistic simulations of bulk a-Si_3N_4 supercells based on first-principles calculations. While these early models were constrained by relatively small system sizes, they laid the groundwork for subsequent studies utilizing significantly larger supercells and statistical ensembles [50, 53, 55–58, 65]. Since the nomenclature of defect sites in a-SiN_x is not always consistent throughout the literature, we adopt the original terminology and refer to undercoordinated Si sites as *K*-centers and use this framework to contextualize different sub-types that were identified in the aforementioned studies.

As outlined in section 3.2.2 and 4.2, a-Si_3N_4 exhibits a broad distribution of bond lengths and bond angles within the amorphous network as well as a low concentration of coordination defects. Depending on the degree of distortion of the local bonding environment, these structural motifs give rise to localized electronic states near the valence- and conduction-band edge, where unoccupied states near the mobility edge of the conduction band act as precursors for electron trapping.

In a-Si_3N_4 supercells generated via MQ-MD, a primary structural feature is the presence undercoordinated Si atoms with three neighboring N atoms (SiN_3), which can serve as a precursor for electron trapping. Structurally, these defects are similar to the nitrogen vacancies in the crystal, though unlike the V_N discussed in section 6.1, individual SiN_3 units occur here in isolation, that match the originally described *K*-centers. Electron trapping at these *K*-centers has been observed in several computational studies [48, 50, 53, 65], where upon charge injection to the simulation cell, the excess electron localizes on the SiN_3 unit. This causes minor structural relaxation towards a pseudo-tetrahedron with the fourth position being occupied by the unpaired electron, see figure 7(a). In the process, the spin moment on the host atom increases from $\approx 0e$ to $0.71e - 0.86e$, while the neighboring atoms remain largely closed-shell, thereby confirming the localized nature of the electron trap.

The CTLs of these traps lie between 0.3 eV and 1.8 eV below the CBM, which is similar to the nitrogen vacancy models in β-Si_3N_4. However, due to the structural disorder of the amorphous phase, the CTLs in a-SiN_x are distributed over a range of $\sim$1 eV and tail out towards lower values as shown in figure 7(e).

Pre-existing *K*-centers are, however, not the only trapping pathways identified in atomistic simulations. As discussed in section 4.2, structurally distorted SiN_4 tetrahedra with widened bond angles can also introduce localized tail states below the CBM. Trapping on these sites further amplifies the existing distortion, lengthening the Si−N bonds and opening the bond angles, while keeping the network

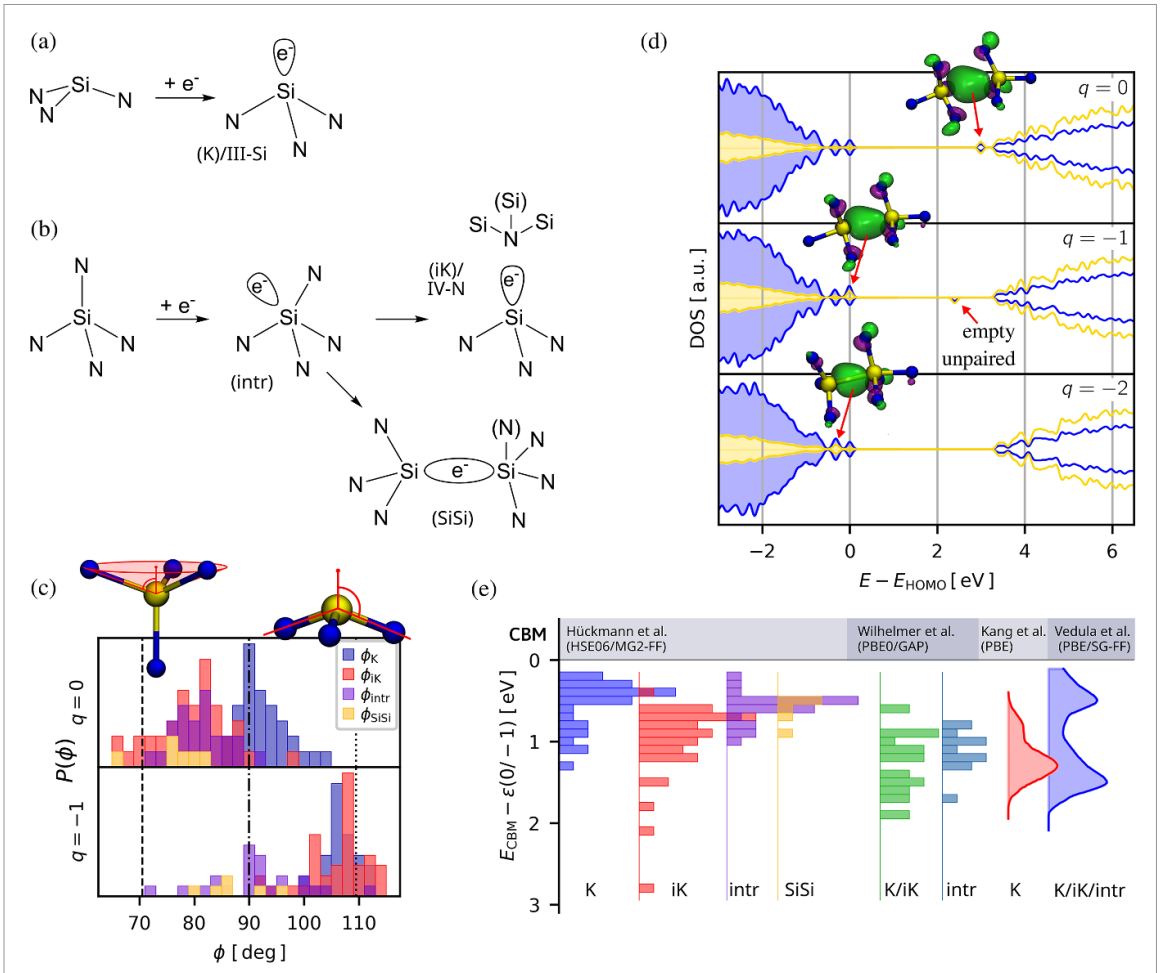

Figure 7. Sketches of electron trapping pathways in a-Si_3N_4: (a) trapping on a K-center (undercoordinated Si atom, III-Si). (b) Trapping on a distorted, fourfold coordinated Si atom resulting in an intrinsic trap (intr), an induced K-center (iK, partially originating form fourfold coordinated N atoms, IV-N), and $N_3Si{-}SiN_{x\in\{3,4\}}$ dumb-bell configurations (Si−Si). Figure adapted from [53]. (c) Relaxation in the amorphous phase measured by the opening angle ϕ of the SiN_4 tetrahedron before and after electron trapping. (d) Projected density of states of nitrogen (blue) and silicon (yellow) relative to the HOMO (E_{HOMO}) in a neutral ($q = 0$), a singly negative ($q = -1$) and doubly negative ($q = -2$) charged supercell with isosurfaces of the empty acceptor precursor state, the single trapped electron, and the doubly occupied trap forming an Si−Si bond. (e) Charge-state transition levels (CTLs) relative to the CBM ($E_{CBM} - \varepsilon(0/-1)$) of recent studies [48, 50, 52, 53, 65]. Figure (a)–(d) Reproduced from [53]. CC BY 4.0.

connectivity intact. Therefore, this trap type has been referred to as intrinsic trap [52, 53] or localized floating states (LFS) in the literature [56, 58]. Structurally, the resulting trap site can be described as a pseudo-trigonal bipyramid, with the electron occupying one of the five positions (figure 7(b)). The extent of the original distortion and the post-trapping configuration can be quantified by the opening angle ϕ of a selected polyhedron face (figure 7(c)). Trapping consistently occurs at sites that are already widened relative to an ideal tetrahedron. Upon electron capture, this distortion is further amplified, with the opening angle partially exceeding 90° in the charged state [53].

In some cases, the structural distortion caused by electron trapping leads to the breaking of a Si−N bond, thereby creating an induced K-center (iK). This bond-breaking process occurs either when the Si−N bond is pre-strained and weakened [51–53], or when the neighboring N atom is overcoordinated and does not give rise to a dangling N site (denoted as IV-N in [48, 65]). Due to the long tail in the bond length distribution, intrinsic traps and induced K-centers cannot be easily distinguished by a single fingerprint, but require careful analysis of the extend of relaxation, coordination numbers before and after electron trapping, and the degree of opening of the coordination polyhedron. Using maximally localized Wannier functions [199], it was demonstrated that the Si and N of the trapping site are covalently bound in the neutral state and break during the localization of an excess electron [46, 52]. The iK-traps are structurally equivalent to native K-centers, adopting a pseudo-tetrahedral geometry, and coincide a significant increase of the opening angle ϕ. The CTLs of the intrinsic traps are located 0.2 eV to 1.8 eV below the CBM, which is in the same range as the K-centers [53]. Since these sites are not related to pre-existing coordination defects structural defect, but rather are introduced by strain, the

charge localization mechanism is of polaronic nature [52], analogous to the polarons observed in crystalline semiconductors.

The third subtype of electron trapping geometries is identified as $N_3Si{-}SiN_{x\in\{3,4\}}$ configurations similar to those described in [55, 66]. In this case, trapping occurs by forming a Si−Si bond where the excess electron is shared between the two Si-atoms. This transition is facilitated by the back-projection of a Si atom towards an adjacent Si neighbor, which does not require a pre-existing dangling bond or V_N defect. The Si−Si trap level lies close to or slightly below the CBM. Due to the small number of $N_3Si{-}SiN_{x\in\{3,4\}}$ configurations in the stoichiometric models, conclusions regarding their statistical significance can only be drawn to a limited extent. The trapping energies fall between the intrinsic electron trap and the trap-induced *K*-center, with an average value of 0.65 eV and a standard deviation of 0.15 eV. This energy distribution is caused by the wide range of Si−Si bond lengths between 2.34 Å to 2.62 Å [53].

When a second electron is injected, it localizes in the same orbital as the first trapped electron independently of the trap type, such that the trap state becomes closed-shell (figure 7(d)). Bipolaron formation triggers the relaxation of the Si atom with the localized electrons towards a nearby Si neighbor, either within the same ring in the network [53] or towards its second-nearest neighbor in a bond switching-like fashion [55]. During this process, a Si−Si bond is formed with the length between 2.22 Å and 2.50 Å [30], which matches the bond length found in crystalline silicon (2.35 Å). The associated electronic state shifts deeper below the LUMO level into the valence band and thus below the N-dominated mid-gap states above the VBM. This implies that upon de-charging, electrons are withdrawn from the N-centered states before the Si−Si bipolarons. The formation of bipolarons thus offers a pathway towards the permanent formation of traps lying deep in the valence band [30, 235]. It remains, however, an open question if and how the these deep traps affect mores shallow trap sites remaining in the band gap and, in extension, if they alter the trapping characteristics. Together, these findings suggest that the trapping of electrons on defective Si-sites exerts a driving force to form Si−Si bonds, though the rigid nature of the *a*-Si_3N_4-network prevents the traps from relaxing spontaneously towards such a configuration. This explains the variety of trapping sites observed as well as the scarcity of $N_3Si{-}SiN_{x\in\{3,4\}}$ traps in the single-electron case.

The atomistic modeling studies discussed so far have primarily focused on stoichiometric *a*-Si_3N_4 occasionally incorporating nitrogen vacancies. This focus was largely dictated by the lack of a classical interaction potential capable of modeling *a*-SiN_x and the larger length-scales required to model Si-rich domains. Experimentally, it is observed that Si-rich *a*-SiN_x has a reduced band gap [58, 169] and exhibits a shift of the trap density profile to more shallow levels [36, 236], which enhances charge carrier mobility presumably by more facile hopping between the trap states. This eases read-write cycles [127, 237], but also enhances lateral leakage, making it a concern for data retention [238].

Theoretical models of *a*-Si_3N_4 containing a nitrogen vacancy suggest that two of the three dangling bonds combine to a Si−Si bond ($3\,N_3Si\cdot \rightarrow N_3Si\text{-}SiN_3 + Si\cdot$) [50]. The binding orbital is fully occupied and its level lies below the LUMO level close to the valence band edge, so that the Si−Si bond neither acts as an electron donor nor acceptor. More recent first principles MQ-MD studies on *a*-SiN_x:H supercells with $1.0 < x < 1.33$ report a closing band-gap as the Si content increases as well as the occurrence of additional mid-gap states, which are scattered over a wider energetic range [56]. Electron trapping in these systems are found to occur on intrinsic traps (denoted as LFS in [56, 58]), that are equivalent to the ones described for the stoichiometric case (figure 7(b)). In the non-stoichiometric case, intrinsic traps localize on mixed $Si(Si_xN_{4-x})$ tetrahedra, indicating that neighboring Si could facilitate local structural rearrangement upon injecting electrons [58]. The structural similarity of the trapping sites and the similar range of levels with respect to the vacuum level suggest that the enhanced charge carrier diffusion stems from the narrowing of the band gap and not from a novel type of traps, though more comprehensive statistical sampling is required to draw final conclusions.

In summary, a series of trapping pathways were identified across the literature, all of which are governed by the interplay of structural distortion in the amorphous network and localization of the associated electronic states. These pathways come down to electrons trapping at localized Anderson states in the band gap, which in turn drives the formation of an Si−Si bond with an adjacent Si neighbor. However, since these localized states can occur not only at defect sites but also at deformed coordination polyhedra, this process is not uniform, which is why various mechanistic pathways have been identified. Likewise, the relatively rigid *a*-Si_3N_4 network prevents the Si−Si bond formation, which is why bond distances corresponding to those in elemental silicon only predominate when trapping two electrons. Overall, the broad variety of trap sites and mechanistic pathways yield similar CTLs and thus a definitive statement over the dominant trapping mode cannot be made.

Table 2. Overview of electron trapping energies in a-SiN_x as obtained by first-principles calculations: charge-state transition level (CTL) with respect to the CBM ($E_{CBM} - \varepsilon(0/-1)$), and the associated band gaps (E_g). The exact CTL distributions are plotted in figure 7(e).

Trapping site	References	Functional	Type	CTL (eV)	E_g (eV)
		β-Si_3N_4			
V_N in β-Si_3N_4-cluster	[123]	B3LYP	hybrid	1.9	
V_N	[124]	BLYP	GGA	1.6	
Si−Si	[124]	BLYP	GGA	1.76	
V_N, Si−Si, Si_N	[126]	B3LYP	hybrid	1.1 − 3.1	5.3
V_N, Si_N	[127]	GW	[a]	1.4	5
		a-Si_3N_4			
K	[50]	PBE/HSE06	GGA/hybrid	1.35 ± 0.15	4.55
K/iK/intr	[48]	PBE	GGA	0.2 − 1.8	3.5 − 4.3
K/iK	[65]	PBE0	hybrid	1.3 ± 0.5	3.8 − 4.6
iK	[52]	PBE0	hybrid	0.77 − 1.66	4.3 − 5.1
K	[53]	HSE06	hybrid	0.24 − 1.27	3.19 − 4.96
intr	[53]	HSE06	hybrid	0.20 − 0.99	3.61 − 4.95
iK	[53]	HSE06	hybrid	0.42 − 1.76	3.66 − 5.03
SiSi	[53]	HSE06	hybrid	0.52 − 0.94	4.22 − 4.93

[a] GW based on perturbation theory on LDA wave function.

6.3. Charge-state transition levels and the band gap problem

Up to this point, we discussed the energetics of intrinsic electron traps with respect to the values reported in the literature, which are summarized in table 2. Although the reported CTLs generally fall within a similar energy range, suggesting that various intrinsic defect types can be classified as deep electron traps, a direct comparison across different studies remains challenging. This is because the reported results are affected by the computational set-up, the stoichiometry of the a-SiN_x samples, the inclusion of hydrogen and the energy references to interpret the defect levels.

Historically, the high computational cost of calculations in large amorphous supercells required the use of GGA functionals, which are known to systematically underestimate the electronic band gap. This shortcoming can, in principle, be mitigated by applying the semi-empirical $+U$ correction. However, this method has to be fitted against experimental data, which is not applicable for a-SiN_x due to the wide spread of band gaps resulting from the different fabrication conditions (see section 3.2.1). Additionally, the commonly used PBE functional tends to underestimate the localization of electronic defect states, limiting its ability to accurately describe localized Anderson states within the band gap. Consequently, the distinction between tail and band states is blurred, which can compromise derived observations such as emission pathways of charge carriers. While the CTLs for $\varepsilon(0/-1)$ derived from GGA calculations often coincide with those obtained from hybrid functional calculation (see table 2), the GGA-based results must be interpreted with caution.

Computational studies nowadays increasingly rely on hybrid-DFT calculations to study the electronic structure. By incorporating a portion of exact Hartree–Fock exchange, these functionals substantially improve both the description of the electronic band gap and the localization of the electronic states. However, even the comparison between hybrid-DFT studies remains difficult. As discussed in section 4.2, the HOMO and LUMO levels are not consistent across different a-Si_3N_4 samples due to the varying nature of local tail states. For single-electron trapping in static calculations, the resulting differences can appear minor as the offset between LUMO and CBM falls within the spread of CTLs that is inherent to the a-Si_3N_4 ensemble. Nevertheless, it must be noted that the values listed in table 2 are strictly speaking not fully comparable without a standardized reference.

To facilitate comparison between different studies and align with the physical picture of delocalized Bloch states, we propose that the mobility edge, rather than the nominal HOMO or LUMO, is a more meaningful reference for defect states in a-Si_3N_4. To analyze carrier transport, charge trapping and emission in the future, identifying the mobility edge in the sample, e.g. via IPR analysis, and consistently distinguishing between localized and delocalized states is essential. Such a distinction would also allow to determine whether capture, transport, and emission mechanisms follow trap-assisted pathways or occur via the conduction band.

6.4. Electron capture cross sections of intrinsic electron traps in *a*-Si_3N_4

With the nature of the various trap sites established, the electron capture process at intrinsic defects can now be analyzed within the NMP formalism as outlined in section 5.2. Here, we will investigate the electron capture properties of intrinsic defects as a representative case study for this framework. First, we will evaluate the PECs in both the neutral and negative charge states to construct the CCD. From these diagram, we will extract the thermal energy barriers and evaluate the electron capture cross sections at room temperature.

A set of supercells with hydrogen-passivated dangling bonds (*a*-Si_3N_4:H) from [52] was chosen for this analysis. We find that the LUMO of these structures are localized at fully coordinated sites in the *a*-Si_3N_4:H supercell, in agreement with the IPR analysis in section 4.2. These sites serve as precursors for electron trapping, and are associated with either an iK or an intrinsic trap as described in section 6.2. The atomic configurations of an exemplaric iK trap and the PDOS in charge states $q = 0$ (left) and $q = -1$ (right) are illustrated in figure 8. The wavefunction of the LUMO state, shown as an isosurface in figure 8(a), is localized on a deformed SiN_4 tetrahedron, where one of the Si-N bonds being on the higher tail end of the bond length distribution at 1.96 Å. The PDOS of this structure is plotted in figure 8(b) for energies around the electronic band gap. This localized unoccupied state at the strained Si–N bond serves as an acceptor for electrons injected from the Si substrate in the conduction band of *a*-Si_3N_4. The localized electron induces structural relaxations, which can even break the strained Si−N bond in case of the iK trap, as illustrated in figure 8(c). As a consequence of the relaxations, the defect state becomes occupied and shifts towards the middle of the band gap (figure 8(d)). Since these trapping sites are not related to any structural defect, but rather are introduced by strain, we previously referred to this charge localization mechanism as polaron formation [52], in analogy to the well-known phenomena in crystalline semiconductors. In this work, we revisit these DFT calculations to evaluate the classical charge transition barriers and calculate the electron capture cross section at room temperature.

As described in section 5.1.1, we consider a delocalized state at the mobility edge as the initial state of the electron capture process. However, the identification of a specific state with the mobility edge remains somewhat arbitrary, considering that the mobility edge in *a*-Si_3N_4 represents a continuous transition rather than a sharp boundary as discussed in section 4.2. Furthermore, the IPR progression near the CBM varies among different amorphous supercells [52]. To ensure comparability throughout our evaluations, we define the mobility edge of each *a*-Si_3N_4:H structure as the first state above the CBM with an IPR value below a threshold of 0.015. This threshold was chosen to ensure that the initial state is consistently delocalized and lies above the energy range where the IPR exhibits fluctuations associated with band-tail states. Due to structural variations, the energy of the initial state ranges from 0.25 eV to 1.5 eV above the LUMO of each respective *a*-Si_3N_4:H sample. We find that this approach gives a physically rigorous description of the capture process, as the total transition probability is predominantly governed by states distributed near the mobility edge, as further discussed below.

First, we construct the CCDs for electron capture from the mobility edge at an intrinsic defects, with an example for the modeled PECs shown in figure 4. To ensure an accurate representation of the energy landscape, we employ hybrid DFT to calculate the energies of initially 12 intermediate, linearly interpolated images between the minimum energy configurations Q_0 and Q_{-1} for each sample. All DFT calculations utilized the same computational setup as presented in [52] to maintain comparability and consistency. The energy of the negative charge state is evaluated up to the energy of the LUMO, as the trapped electron begins to delocalize when the system is elevated above this state. In the neutral charge state, we additionally sample the energies into the negative Q regime up to the crossing point of the parabolas. We find that some PECs of the analyzed defects exhibit non-harmonic behavior in the neutral charge states, which treatment is beyond the scope of this work. In the following, we therefore restrict our analysis to trapping sites where the parabolic fit $E^q(Q)$ yields a coefficient of determination of $R^2 \geqslant 0.99$ for both charge states.

The classical energy barriers for electron capture $E_b^{0/-1}$ and emission $E_b^{-1/0}$ were extracted from the crossing point of the PECs and are plotted as a function of the thermodynamic trap level E_T in figure 9(a). In this plot, each data point corresponds to the electron trapping properties of a different *a*-Si_3N_4:H structure. The trap levels of the nine investigated harmonic intrinsic electron traps are $1.05 - 2.40$ eV below the mobility edge.

The crossing points of all evaluated CCDs lie close to the minimum energy configuration in the neutral charge state, similar to the illustration in figure 4. Consequently, the electron capture barriers are small, ranging from only 1 meV to 252 meV. We further evaluate the phonon energies associated with the effective modes of the electron capture process, which range from 30 meV to 62 meV for the investigated trapping sites. Therefore, we find that the thermal activation barrier $E_b^{0/-1}$ corresponds to only a few

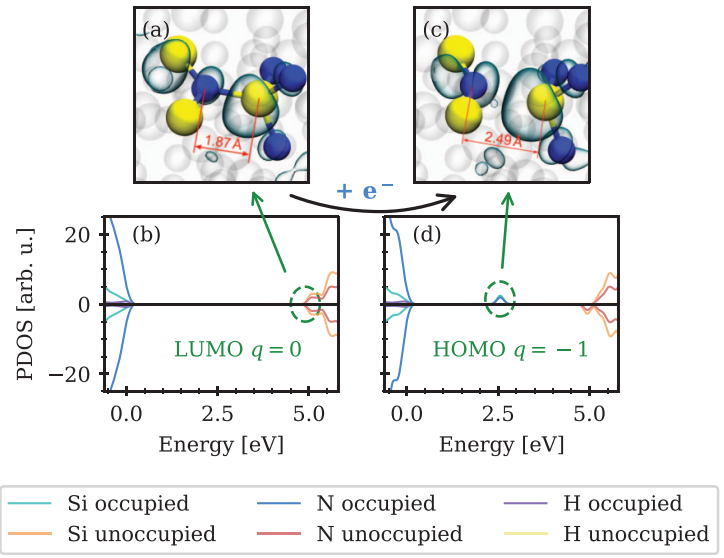

Figure 8. Electron trapping at an iK defect in the amorphous a-Si_3N_4:H network. (a) Atomic structure of a strained Si–N bond in the neutral charge state with the localized defect wave function corresponding to the lowest unoccupied molecular orbital (LUMO). (b) Corresponding projected density of states (PDOS) of the neutral a-Si_3N_4:H structure. The energy of the defect state (LUMO) is at the bottom of the conduction band. (c) Same atomic site with a trapped electron, corresponding to the highest occupied molecular orbital (HOMO) of the negatively charged structure. After addition of the electron, the strained bond breaks, causing the Si–N distance to widen from 1.96 Å to 2.86 Å. (d) PDOS of the negatively charges a-Si_3N_4:H structure. The state at the conduction band, now occupied (HOMO), is shifted to the middle of the band gap due to the structural relaxations. Reprinted (figure) with permission from [52], Copyright (2024) by the American Physical Society.

phonons of the effective mode at most. Since the thermal energy at room temperature is sufficient to overcome these barriers, rapid electron capture rates are expected. On the contrary, the energy barriers for electron emission from the defect to the CBM naturally increase with E_T and range between 1.05 eV and 2.65 eV, suggesting that thermal de-trapping back to the conduction band is highly unlikely.

Subsequently, the electron capture cross sections of the intrinsic trapping sites are calculated using equation (11). The capture cross sections $\sigma_{0/-1}$ in log-scale are plotted against the thermal activation barriers $E_b^{0/-1}$ in figure 9(b). Our evaluations demonstrate that already minor deviations in the CCD, and consequently $E_b^{0/-1}$, can change the charge capture probability of a trapping site by orders of magnitude. The evaluated capture cross sections vary between $6 \times 10^{-18} - 3 \times 10^{-13}\,\mathrm{cm}^2$ at $T = 293\,\mathrm{K}$, which is within the typical range of deep level defects in semiconductors [69].

Additionally, the calculated $\sigma_{0/-1}$ compare well with capture cross sections employed for device-scale simulations to model the program, erase or retention characteristics of CTFs [78, 79, 127, 239–241]. In these studies, typically a fixed $\sigma_{0/-1}$ for all traps is assumed, with values ranging between $10^{-18} - 10^{-13}\,\mathrm{cm}^2$ depending on the specific model calibration. It is worth noting that the choice of $\sigma_{0/-1}$ in device simulations is often coupled to other employed parameters like the trap density or the trap level. Considering the inherent challenges of evaluating $\sigma_{0/-1}$ with DFT as discussed in section 5.2, we find that our calculations align with the empirical ranges used in literature. Furthermore, the wide variance in our calculated $\sigma_{0/-1}$ emphasizes that a distribution of trap parameters should be employed in future device modeling studies to account for variations in defect properties inherent to a-Si_3N_4 thin films.

While we have focused our calculations of $\sigma_{0/-1}$ on electron exchange with the estimated mobility edge, the electron can, in principle, also be captured from states higher in the conduction band. Such states may become occupied during the CTF programming cycle at high positive gate bias (compare with figure 1(a)), and can therefore also serve as initial states of the transition. However, these high-energy electrons typically thermalize rapidly into empty, lower-energy delocalized states, thereby reducing their probability to be directly captured at intrinsic defects. Furthermore, we also expect $\sigma_{0/-1}$ to be smaller for high energy states than for states at the mobility edge, which can be directly understood from the discussion in section 5.2. In the CCD, a higher initial state simply corresponds to a vertical shift of the neutral PEC, as indicated by the displaced parabolas in figure 4. Assuming that both the state at the mobility edge and the states above are delocalized, also the overlap with the final wave functions in equation (11) remains largely unchanged. Crucially, as the energy of the initial state ϵ_i increases, both the electronic energy difference in $|\epsilon_f - \epsilon_i|^2$ and likewise the thermal barrier $E_b^{0/-1}$ equation (5) increase.

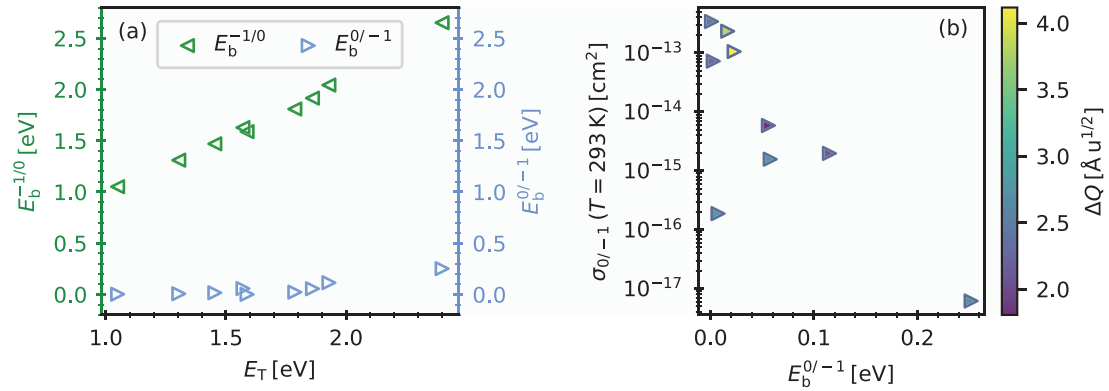

Figure 9. Calculated capture and emission properties for the nonradiative multiphonon transition of an electron between the mobility edge and an intrinsic electron trap. The scatter plots show the properties of nine defects, each of them located in a different a-Si_3N_4:H sample structure. (a) Classical energy barriers for electron emission $E_b^{-1/0}$ (left) and electron capture $E_b^{0/-1}$ (right) vs. the trap level E_T with respect to the mobility edge. (b) Electron capture cross section $\sigma_{0/-1}$ evaluated at room temperature ($T = 293$ K) as a function of $E_b^{0/-1}$. The color bar gives the total configuration coordinate change of the respective transition.

Although $\sigma_{0/-1}$ scales quadratically with the energy difference, it is simultaneously suppressed by the Arrhenius-factor $\exp\left(-E_b^{0/-1}/k_BT\right)$. At room temperature ($k_BT \approx 25$ meV), this exponential decay quickly dominates $\sigma_{0/-1}$, leading to a net reduction of the transition rate for higher initial energies. Our first-principles evaluations therefore suggest that electron trapping stems from states close to the mobility edge. However, a complete description of CTF transition rates would require full device simulations to account for the steady-state electron distribution induced by tunneling from the Si substrate (section 2).

6.5. Experimental characterization of charge traps in a-Si_3N_4

Experimental identification of specific trapping sites in a-SiN_x is inherently challenging due to the broad distributions of bond lengths, bond angles and coordination numbers in the amorphous network. Nevertheless, the overall electron trap level distribution and trap density in a-SiN_x has been evaluated in several studies, typically without assigning the trapped electrons to specific atomic configurations. The extracted trap level distributions vary slightly across different works, which is not only attributed to the different characterization methods employed, but also to the varying growing techniques and exact stoichiometries of the thin films, both of which fundamentally impact the structural and trapping properties (see section 3.2). The electron trap levels extracted from experiment and device-level simulations range from $0.6 - 2$ eV below the CBM [36, 37, 39, 42, 66, 85, 86, 126, 242–246], giving an overall good agreement with the first-principles energy levels for the various trapping sites summarized in table 2 and illustrated in figure 7.

In particular, various studies suggest that the Si content in the silicon nitride has a large impact on the charge storage behavior. Figure 10(a) illustrates the electronic bandgap of a-SiN_x as a function of the N/Si ratio [58] as measured with reflection electron energy loss spectroscopy (REELS). A strong decrease of the band gap with increasing Si content is thereby revealed, which aligns with the introduction of in-gap states with increasing Si content as predicted by first-principles calculations [56]. In [36], the spatial trap densities of ONO stacks with Si-rich and stoichiometric silicon nitride layers were extracted from capacitance–voltage (C–V) measurements, indicating that the Si-content in the nitride has a surprisingly small impact on the overall trap density (9.5×10^{18} cm^{-3} for the stoichiometric sample vs. 9.0×10^{18} cm^{-3} for the Si-rich sample). However, by modeling the retention characteristics over time at $T = 200\,^\circ$C, it was found that Si-rich silicon nitride has a higher density of traps in relatively shallower energy levels, as shown in figure 10(b) [36]. These shallower states align with the observed narrowing of the band gap with higher Si-content.

A similar trend was reported in [37], where the peak of the electron trap distribution of Si-rich samples was found to be approximately 0.2 eV shallower than in stoichiometric SiN. Consequently, the retention of the Si-rich sample was found to be worse compared to that of SiN across the entire investigated temperature range ($25 - 200\,^\circ$C). The shift toward shallower trap levels is presumably attributed to a higher density of Si–Si bonds in the Si-rich samples, as discussed in section 6.2. The corresponding trap density spectrum of SiN in a TANOS stack, as obtained with TSCIS, is shown in figure 10(c) [37].

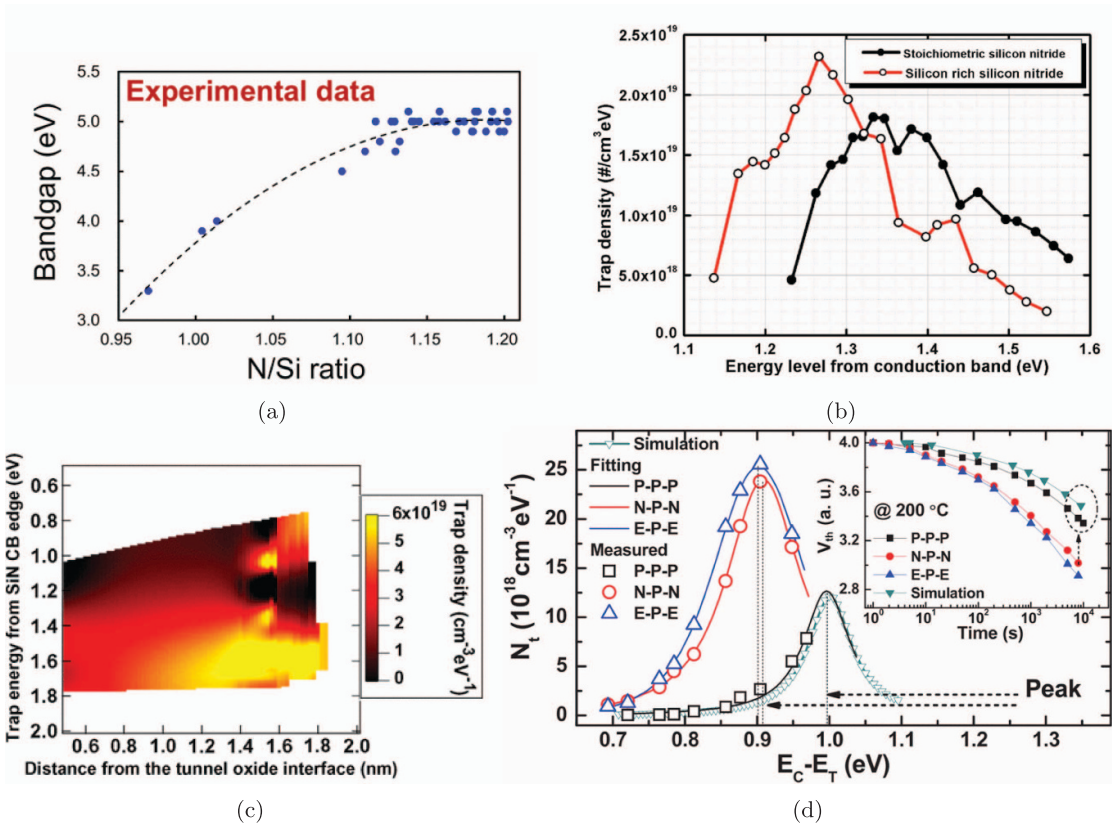

Figure 10. Experimentally evaluated electron trapping characteristics in amorphous silicon nitride. (a) Electronic band gaps of a-SiN_x obtained with REELS for varying N/Si ratios. Reproduced from [58]. CC BY 4.0. (b) Trap level distribution extracted from the retention characteristics of SONOS stacks. Reprinted from [36], with the permission of AIP Publishing. (c) Trap density spectrum of SiN in a TANOS stack obtained with the charge injection and sensing technique. © (2010) IEEE. Reprinted, with permission, from [37]. (d) Trap level distribution extracted from retention characteristics of 3D NAND flash cells, where each cell is operated in a different mode (program (P), neutral (N), erase (E)). The inset shows the threshold voltage shift of the programmed cell over time at $T = 200\,^{\circ}$C. Reproduced with permission from [39]. © 2015 The Japan Society of Applied Physics.

The spectrum reveals a trap density peak at ≈1.6 eV with trap densities exceeding $10^{19}\,\mathrm{cm}^{-3}\,\mathrm{eV}^{-1}$. Furthermore, the extracted spectrum indicates a higher trap density farther from the interface to the tunnel oxide, which aligns with the spatial trap distribution used to simulate retention transient measurements in the same study. This is likely attributed to the high kinetic energy of the injected electrons, as discussed in section 2. It should be noted that the trapping parameters in this study were extracted according to the SRH model, and are thus only roughly comparable with the CTLs evaluated with the NMP model in table 2.

The trap level distribution obtained from the retention characteristics of 3D NAND flash cells at $T = 200\,^{\circ}$C are shown in figure 10(d) [39]. In this study, the retention of adjacent cells was measured and simulated to extract the trap density for different operation states of each cell, program (P), neutral (N) and erase (E). When all three cells of the device are programmed (P–P–P), the threshold voltage shift over time due to lateral electron diffusion is suppressed by the electrons stored in adjacent cells. Using 3D TCAD simulations, a trap level distribution with a peak at 1 eV below the CBM was extracted, showing a density of $\sim 10^{19}\,\mathrm{cm}^{-3}\,\mathrm{eV}^{-1}$. This aligns with TCAD simulations of CTF devices in other works, which suggest a trap density in the silicon nitride storage layer in the range of $10^{19} - 10^{20}\,\mathrm{cm}^{-3}$ [78, 247, 248].

In [245], band gaps between 5.1 eV and 5.4 eV were obtained for samples fabricated by PECVD and sputtering, highlighting again the sensitivity of the electronic structure with respect to the fabrication methodology as discussed in section 3.2.1. Various spectroscopy measurements [63, 243, 245] suggest that the electron trapping levels are distributed down to approximately 1.6 eV below the CBM. Based on the obtained energy peaks from REELS and spectroscopic ellipsometry (SE), tentative transition models have been proposed. However, a definite assignment of the photoluminescence (PL) spectra to specific defect transitions has not yet been achieved. First-principles evaluations of the line shape functions for optical transitions between the CBM, the VBM and internal defect levels could guide the identification of these observed spectra with specific trapping sites [68, 249].

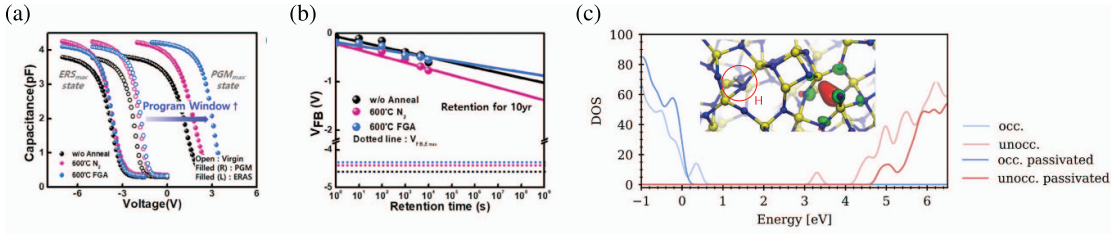

Figure 11. *C–V* measurement of memory characteristics of a Si-rich ONO capacitors annealed in pure N_2 (pink) and N_2/H_2 atmosphere (blue). (a) Memory window and [259] (b) retention characteristics. The dotted line represents the flat band voltage (V_{FB}) at the maximum erased state. (a) and (b) reproduced from [259]. CC BY 4.0. (c) Density of states (DOS) of a representative *a*-Si_3N_4:H supercell calculated with PBE0_TC_LRC showing the occupied and unoccupied states before and after H passivation. Reprinted (figure) with permission from [52], Copyright (2024) by the American Physical Society. Inset: Representative example of the localized state on a Si atom formed independently from the N–H site in the neutral charge state. Si is colored in yellow, N is blue, and H is gray. The respective spin channels are colored red and green. Reproduced from [54]. CC BY 4.0.

6.6. The role of common impurities on charge trapping

Silicon nitride is susceptible to the incorporation of a broad range of impurities (H, O [250], Al [251], Ti [63], B [64]), either through the fabrication process, deliberate doping, or during device operation when embedded in a multicomponent material stack. Among these, hydrogen and oxygen are arguably the most critical, as neither can be fully avoided (H from fabrication, O from embedding in SONOS stacks) and, given their reactivity, are expected to interact with defect sites that facilitate charge trapping. Accordingly, both impurities were studied in depth and will be summarized in the following.

6.6.1. Hydrogen

As discussed in section 3.2, hydrogen is inherently incorporated in *a*-SiN_x films, particularly when grown by plasma-enhanced deposition techniques. Although its concentration can be reduced through high-temperature annealing, and low-hydrogen growth protocols exist [116, 145], residual hydrogen is generally difficult to avoid completely and must be considered when discussing charge-trapping mechanisms.

In general, hydrogen acts as a passivating agent for undercoordinated Si and N defects by forming Si−H and N−H bonds [252, 253] according to

$$N_3Si\cdot + H\cdot \longrightarrow N_3Si{-}H \tag{17a}$$

$$Si_2N\cdot + H\cdot \longrightarrow Si_2N{-}H. \tag{17b}$$

Importantly, some intrinsic traps such as induced *K*-centers do not require pre-existing dangling bonds, and charge trapping in *a*-Si_3N_4 is therefore still observed even if, hypothetically, all *K*-centers in the sample are passivated by hydrogen (see section 6.2). This is supported by EPR measurements in hydrogen plasma annealed *a*-SiN_x films, which reveal spin densities on the order of $10^{18}\,cm^{-3}$ [254]. Furthermore, PL studies indicate the presence of electronic states within the band gap, with optical transitions comparable to those in films with low H content [255, 256].

Annealing *a*-SiN_x films in a N_2/H_2 atmosphere has been reported to reduce the overall trap density, accompanied by a shift toward energetically deeper trap states. This modification typically results in a narrower memory window and improved data retention, suggesting that post-deposition annealing may provide a means to tune the trapping characteristics [257–259]. The effects of annealing is generally more pronounced in silicon-rich SiN_x films, consistent with their higher initial defect density and the correspondingly greater potential for defect passivation [256, 259]. However, similar improvements in retention and trap redistribution are also observed after annealing in pure N_2 atmosphere [257, 260], see figures 11(a) and (b), although long-term data retention measurements are required to draw final conclusions. Especially the *C–V* curves are often insensitive to whether annealing contains H_2. This indicates that the dominant mechanism is likely thermally activated defect reconfiguration and structural relaxation, whereas hydrogen primarily contributes through passivation of pre-existing coordination defects. Consequently, parameters such as stoichiometry and intrinsic defect concentration appear to exert a more decisive influence on the charge trapping behavior than hydrogen incorporation. It remains therefore an open question whether hydrogen treatment affects the device performance beyond the chemical stability of the material [259, 260].

DFT calculations confirm that in the presence of coordination defects, hydrogen passivates undercoordinated atoms in accordance with equation (17*b*) and removes their associated electronic state from the band gap [52], see figure 11(c). Otherwise, hydrogen binds to adjacent NSi_3 or SiN_4 units

with either protonic (H^+) or hydridic (H^-) character without introducing additional states within the band gap [54]. Thus, H acts as acceptor or donor depending on whether it is adjacent to a Si or N atom donor, respectively. The corresponding H-related states are located deep within the valence band, while the band edges remain dominated by the intrinsic states of the pristine a-Si_3N_4 network. Consequently, H has no effect on the trapping characteristics. An exception to the mostly idle behavior of H arises in the presence of pre-strained or elongated Si-N bonds. Analogous to the creation of hydroxyl E' defects in a-SiO_2 [60, 261–265], hydrogen can cause bond rupture ($Si_2N-SiN_3+H\cdot \rightarrow Si_2-N\cdot +N_3Si-H$), thereby generating new dangling bonds [54]. This newly formed coordination defect is structurally and electronically analogous to native N-dominated defect states near the VBM and its electronic activity depends primarily on its energetic position relative to the band edges. Based on FT-IR measurements, a similar mechanism involving H insertion into weak Si−Si bonds and the formation of an Si-H-Si configuration has recently been proposed [266].

While hydrogen can passivate existing defects and remove states from the band gap, it may also locally disrupt the amorphous network and create new coordination defects. Importantly, the hydrogen atom itself does not introduce intrinsic mid-gap states; rather, any electronic activity arises indirectly through the resulting defect restructuring. Based on the findings, data retention appears to be largely insensitive to hydrogen concentration, as the observed modifications in trap density and depth distribution remain dictated by the complex interplay of stoichiometry and defect concentration (see figures 11(a) and (b)). Consequently, for applications in CTF devices, hydrogen passivation primarily enhances the chemical stability of the dielectric by eliminating reactive coordination defects, without fundamentally altering the intrinsic trapping characteristics. The persistent observation of charge trapping despite defect passivation lends further support to the intrinsic trapping mechanism described in section 6.2 and several recent first-principles studies [46, 52, 53, 58].

6.6.2. Oxygen

In contrast to the relatively passive role of hydrogen, oxygen has been shown to fundamentally modify the electronic structure of a-SiN_x and thus plays a critical role for its charge-trapping characteristics. Although a-SiN_x is known for its high oxidation resistance, defective as-deposited PE-CVD and PE-ALD films undergo limited oxidation upon exposure to ambient conditions [145, 267]. In multilayer SONOS memory stacks, thermally activated interfacial reactions during post-deposition annealing promote the formation of silicon oxynitride (SiN_xO_y) at the a-SiN_x/a-SiO_2 interface, which can lead to a graded, depth-dependent oxygen concentration profile [268]. Beyond unintentional incorporation, SiN_xO_y can also be deliberately synthesized by introducing oxygen-containing precursor species (e.g., N_2O or NO) during deposition, enabling the systematic tuning of structural, electronic, and trapping properties [269].

In this context, the distinction between oxygen-doped silicon nitride (a-SiN_x:O) and silicon oxynitride is not rigorously defined. Because nitrogen and oxygen can be incorporated in the amorphous Si-O-N network over a continuous compositional range, oxygen-doped a-SiN_x cannot be separated from SiN_xO_y. Instead, the material system spans a continuum from nitride-rich compositions with minor oxygen incorporation to oxide-rich oxynitride networks. In the following, we therefore treat the emerging trends associated with O-incorporation as a function of the oxygen concentration and discuss their implications for CTF devices.

The chemical composition and local bonding configurations of a-SiN_x:O have been characterized by Fourier-transform infrared (FT-IR) spectroscopy and x-ray photoelectron spectroscopy (XPS). In FT-IR spectra, the Si−N and Si−O stretching modes appear in the range of 830 to 900 cm^{-1} and 1040 to 1100 cm^{-1}, respectively [270, 271]. In oxynitride films, these contributions partially overlap, forming a broad composite absorption band due to structural disorder and mixed bonding environments. Although the vibrational frequencies vary moderately with local coordination, the centroid of the combined band shifts systematically toward higher wavenumbers with increasing oxygen concentration, signaling the evolution from nitride-like toward oxide-like bonding characteristics [272].

In XPS spectra, the Si 2p core level is sensitive to the local coordination environment, shifting systematically with the number of N and O neighbors. The binding energy of the Si 2p level in a-Si_3N_4 is around 101.9 eV [273], which shifts to 103.6 eV for a-SiO_2 [274]. For intermediate compositions, SiN_xO_y films show a single, broadened Si 2p peak positioned between these two limits (see figure 12(a)). This behavior is consistent with a CRN composed of mixed $SiN_{4-x}O_x$ tetrahedra with $x \in [0,4]$ [272, 275, 276]. While minor asymmetries in the peak shape and fitting weights may deviate from an ideal stochastic distribution of $SiN_{4-x}O_x$ tetrahedra, indicating the presence of oxygen- and nitrogen-rich domains, compositional inhomogeneities are less pronounced than those observed for $SiN_{x<1.33}$ [174] or $SiO_{x<2}$ [277]. In agreement with FT-IR analysis, these findings support the description of SiN_xO_y as a CRN of mixed $SiN_{4-x}O_x$ tetrahedra with limited phase separation.

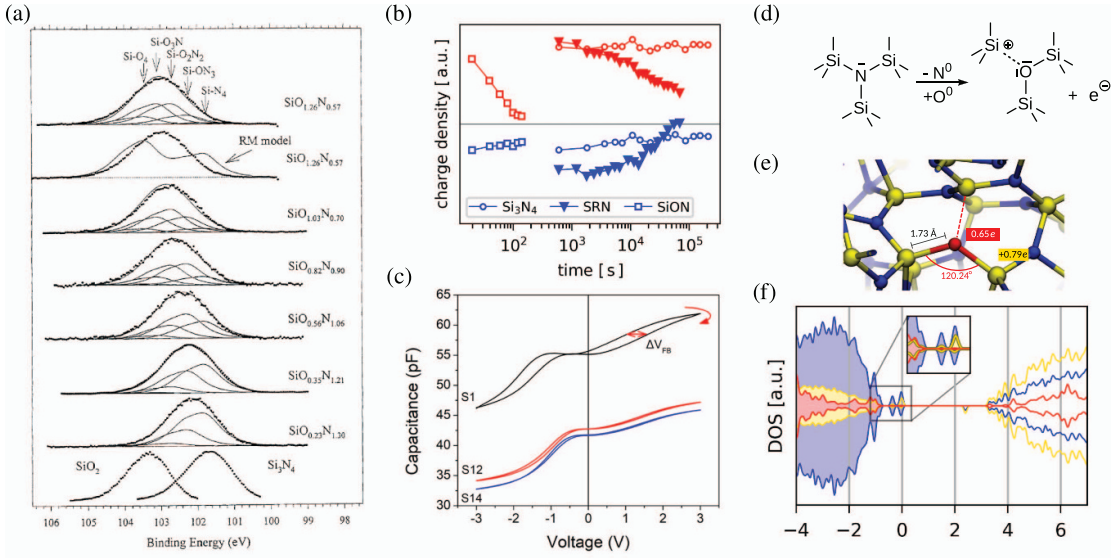

Figure 12. (a) Si 2*p* XPS spectra of SiN_xO_y films with various O:N ratios. The fits (solid lines) are decomposed into contributions of the $SiN_{4-x}O_x$, $x \in [0, 4]$ tetrahedra. Reprinted from [275], Copyright (2002), with permission from Elsevier. (b) Charge decay line profile over time measured by electrostatic force microscopy at 250 °C for stoichiometric *a*-Si_3N_4, silicon-rich nitride (SRN), and silicon oxynitride (SiON). The electrons are colored blue, the holes are red. Data replotted from [278]. (c) *C*–*V* curve measured for pristine *a*-Si_3N_4 (S1), 120 s (S12), and 240 s (S14) plasma doped *a*-Si_3N_4:O. © (2021) IEEE. Reprinted, with permission, from [279]. (d)/(e) Schematic and ball-and-stick model of oxygen substitution defects in *a*-Si_3N_4. (f) The projected density of states (PDOS) relative to the Fermi level of silicon (yellow), nitrogen (blue), and oxygen (red) for an isolated oxygen substitution defect in *a*-Si_3N_4. Obtained from DFT calculations at HSE06 level. (d)–(f) are Reproduced from [62]. CC BY 4.0.

Regarding the electronic structure, it is well documented that even trace concentrations of oxygen impurities can significantly alter the device performance [279–283]. With increasing oxygen content, the band gap of the material widens from approximately $4.6 - 5.5\,\text{eV}$ in pristine *a*-Si_3N_4 to about $8 - 9\,\text{eV}$ for pure *a*-SiO_2, with SiN_xO_y values falling in between these two extremes depending on the oxygen content [107, 284–287]. At the same time, gap states associated with Si dangling bonds shift by approximately 0.15 eV, settling at 3.12 eV above the VBM. Additional gap states attributed to Si-O-Si and N-Si-O configurations are also observed near the valence band edge [288–290].

The incorporation of oxygen reduces the trap density by passivating defective sites responsible for deep traps in pristine *a*-SiN_x. Consequently, the distribution of trap states shifts to energy levels closer to the mobility edge [10, 271]. While this enhances charge-carrier mobility via thermally assisted hopping, it can also promote lateral and vertical leakage. This can negatively impact data retention [291], as demonstrated by the rapid charge density decay in SiN_xO_y films as shown in figure 12(b) [278]. Conversely, the presence of oxygen reduces hysteresis in *C*–*V* measurements [279], allowing easier memory write and erase operations (figure 12(c)). Ultimately, whether oxygen incorporation is a net benefit for fine-tuning CTF devices remains a topic of ongoing debate [38, 279, 287, 292–295].

Atomistic modeling of *a*-SiN_x:O could provide insights into the influence of the O content on the charge trapping properties. First computational models of oxygen substitution defects (O_N) in crystalline β-Si_3N_4 reveal that these defects introduce mid-gap states slightly above those associated with *K*-centers. Because oxygen possesses one more valence electron than nitrogen, the O_N center effectively acts as a donor to lower-lying states, replacing a silicon-centered two-electron trap with a shallower, oxygen-related single-electron trap ($O_N \rightarrow O_N^+ + e^-$) [296, 297].

In the amorphous phase, O_N defects relax into a silica-like Si-O-Si configuration, as illustrated in figure 12(d), thereby formally creating a dangling Si bond due to the lower valency of oxygen compared to nitrogen [62]. While this site structurally resembles a *K*-center in pristine *a*-Si_3N_4, analyses of the spin density and PDOS indicate that these oxygen-induced *K*-centers do not contribute to the edge states responsible for charge trapping unless significant local structural rearrangement occurs (figures 12(e) and (f)). This is explained by the negatively polarized O_N, which stabilizes the defective site via Coulomb interaction, resulting in defect states that lie above the native mid-gap states and closer to the mobility edge of the conduction band.

These results suggest that electron trapping and the charge-state transition levels remain primarily governed by the native traps in *a*-Si_3N_4. The O_N defect effectively acts as a donor that promotes the

population of deep traps, even though the oxygen atom formally exists in the O^{2-} state. Effectively, O defects facilitates the occupation of deep traps while creating new, more shallow ones due to the stabilizing interaction of the O atom with nearby N_3Si^+ sites. This finding is consistent with the systematic shift in the trap profile for SiN_xO_y films towards more shallow levels and the resulting increase of charge carrier mobility.

It must be noted that current computational models typically only focus on the dilute limit and are therefore not fully representative of SiN_xO_y systems. While isolated oxygen atoms can stabilize adjacent *K*-centers and shift their associated mid-gap states toward the band edges, which is consistent with the experimentally observed increase in charge-carrier mobility in oxygen-containing nitride films, these dilute models do not yet account for the widening of the band gap. Therefore, conclusions regarding oxynitrides with substantial O content should be drawn with caution.

7. Conclusions and perspective

In this review, we have provided a comprehensive discussion on the microscopic origins of electron localization in the amorphous silicon nitride storage layer of CTF memory devices. First-principles calculations, device-level simulations and experimental characterizations reveal a broad distribution of deep electron trap levels in *a*-SiN_x. We conclude that these states are introduced by a variety of structural irregularities in the amorphous network, including coordination defects, strained bonds, Si–Si bonds, dangling bonds and impurities. Consequently, the charge retention capabilities are highly sensitive to the stoichiometry and the deposition conditions of the *a*-SiN_x thin films.

As a representative demonstration of the underlying physics, we have calculated classical charge transition barriers and capture cross sections of intrinsic electron traps based on the NMP transition model. The calculated electron capture cross sections range from $6 \times 10^{-18} - 3 \times 10^{-13}\,\mathrm{cm}^2$ at $T = 293\,\mathrm{K}$ and offer a physical framework that aligns with the parameter ranges used in previous device simulations, providing an atomistic description for the macroscopic models employed in the field. Our calculations further suggest that thermal emission of electrons from the trapping site to the conduction band has a low probability, in agreement with the long charge retention times observed in *a*-Si_3N_4-based CTF devices.

However, the trap properties evaluated through these methods can only be used to understand the general charge trapping capabilities of a defect, as the total electron localization rate in a device depends heavily on operating conditions. In particular, the lateral distribution of the electrons injected in the nitride layer and their local density significantly influence the programming rate. These parameters are affected by the tunneling rate, and are thus sensitive to the device geometry and applied bias. A comprehensive understanding of the microscopic transition rates in CTF devices therefore requires device-level simulations that explicitly account for spatial charge density, internal field distributions, and bias-dependent tunneling. Moreover, these analyses need to be carried out over a wide temperature range to account for electron–phonon scattering and the temperature dependence of the capture coefficient. Looking forward, the evaluation of the capture cross section should be extended to cryogenic temperatures which will require the treatment of vibrational tunneling effects.

While this work focuses strictly on the electron capture process, a comprehensive model of CTF performance and reliability must also account for hole trapping mechanisms, in particular when analyzing erase and retention characteristics, where electron- and hole-capture regimes cannot be treated as decoupled processes. Recent first-principles calculations indicate that excess holes localize at distinct structural defects such as undercoordinated N [48, 53, 65] or form large hole polarons across adjacent fully coordinated N sites [52]. The calculated hole trap levels of these sites are tendentiously shallower than those of the deep electron traps, making them highly relevant for charge compensation during the erase cycle. The non-radiative multiphonon transition pathways for hole localization in *a*-Si_3N_4 likely differ significantly from their electron counterparts and must be evaluated independently. While an analysis of hole kinetics is outside of the scope of this study, characterizing these complementary mechanisms is a crucial step toward a fully physics-based TCAD framework for flash memories.

Additionally, it is suggested by DFT that the trapping levels of Si–Si sites shift toward the VBM with increasing Si content, which should make the electron traps deeper [58]. However, since the band gap is simultaneously decreasing with higher N/Si ratios, the electron trap levels effectively might become shallower when related to the CBM, aligning with experimental observations. To validate this trend, larger statistics of samples with various Si contents are needed.

Finally, as device dimensions continue to shrink, fluctuations of the charge density and local field effects are expected to become more pronounced and might critically influence the long-term device

reliability. In this context, phenomena such as trap-assisted tunneling or polaron hopping, which are not fully captured by static transition models, need to be understood in detail to describe lateral electron diffusion. Addressing these challenges is essential for establishing predictive frameworks that connect microscopic defect physics to the macroscopic performance and degradation of next-generation CTF technologies.

Acknowledgments

Calculations were performed using supercomputer resources provided by the Vienna Scientific Cluster (VSC).

Data availability statement

The data cannot be made publicly available upon publication because the cost of preparing, depositing and hosting the data would be prohibitive within the terms of this research project. The data that support the findings of this study are available upon reasonable request from the authors.

Funding

This project has received funding from the European Research Council (ERC) under Grant Agreement No. 101055379 (F2GO). Additionally, this research is co-financed by Holland High Tech through a public-private partnership in research and development within the Dutch top sector of High-Tech Systems and Materials (HTSM). The authors acknowledge TU Wien Bibliothek for financial support through its Open Access Funding Programme.

Author contributions

Christoph Wilhelmer 0000-0002-9996-2589
Conceptualization (lead), Data curation (lead), Formal analysis (lead), Investigation (lead), Methodology (lead), Project administration (lead), Validation (equal), Visualization (lead), Writing – original draft (lead)

Lukas Hückmann 0000-0003-4718-4604
Conceptualization (lead), Data curation (lead), Formal analysis (lead), Investigation (supporting), Methodology (lead), Project administration (supporting), Validation (equal), Visualization (lead), Writing – original draft (lead)

Jonathon Cottom 0000-0002-5918-9464
Formal analysis (equal), Validation (lead), Writing – review & editing (equal)

Dominic Waldhoer 0000-0002-8631-5681
Formal analysis (equal), Validation (lead), Writing – review & editing (equal)

Jörg Meyer 0000-0003-0146-730X
Funding acquisition (lead), Resources (equal), Supervision (equal), Validation (equal), Writing – review & editing (equal)

Tibor Grasser 0000-0001-6536-2238
Funding acquisition (lead), Resources (equal), Supervision (equal), Validation (equal), Writing – review & editing (equal)

References

[1] Sze S M, Li Y and Ng K K 2021 *Physics of Semiconductor Devices* (Wiley)
[2] Jagan S M *et al* 2014 Umesh Chand and Tseung-Yuen Tseng. Overview of emerging nonvolatile memory technologies *Nanoscale Res. Lett.* **9** 526
[3] Barta J, Manela M and Fischer R 1985 Si_3N_4 and Si_2N_2O for high performance radomes *Mater. Sci. Eng.* **71** 265–72
[4] Okada A 2008 Automotive and industrial applications of structural ceramics in japan *J. Eur. Ceram. Soc.* **28** 1097–104

[5] Li X et al 2009 Mechanical and dielectric properties of porous $Si_3N_4-SiO_2$ composite ceramics *Mater. Sci. Eng. A* **500** 63–69
[6] Hongli D, Yan Li and Chuanbao C 2010 Effect of temperature on dielectric properties of Si_3N_4/SiO_2 composite and silica ceramic *J. Alloys Compd.* **503** L9–L13
[7] Vila M et al 2003 Mechanical properties of sputtered silicon nitride thin films *J. Appl. Phys.* **94** 7868
[8] Xingjie D et al 2022 Additive manufacturing of silicon nitride ceramics: a review of advances and perspectives *Int. J. Appl. Ceram. Technol.* **19** 2929–49
[9] Liu H W, Su H P, Lai W K and Cheng H C 1997 The oxidation mechanism of low pressure dry oxidation of nitrides for memory devices *J. Electrochem. Soc.* **144** 3288
[10] Wrazien S J, Zhao Y, Krayer J D and White M H 2003 Characterization of SONOS oxynitride nonvolatile semiconductor memory devices *Solid-State Electron.* **47** 885–91
[11] Wang L., Yang C. H. and Wen J 2015 Physical principles and current status of emerging non-volatile solid state memories *Electron. Mater. Lett.* **11** 505–43
[12] Doo V Y, Nichols D R and Silvey G A 1966 Preparation and properties of pyrolytic silicon nitride *J. Electrochem. Soc.* **113** 1279
[13] Törmä P T et al 2013 Ultra-thin silicon nitride x-ray windows *IEEE Trans. Nucl. Sci.* **60** 1311–14
[14] Törmä P T et al 2014 Performance and properties of ultra-thin silicon nitride x-ray windows *IEEE Trans. Nucl. Sci.* **61** 695–99
[15] Cornaby S and Bilderback D H 2008 Silicon nitride transmission x-ray mirrors *J. Synchrotron Rad.* **15** 371–73
[16] Sacher W D, Huang Y, Ding L, Barwicz T, Mikkelsen J C, Taylor B J F, Lo G Q and Poon J K S 2014 Polarization rotator-splitters and controllers in a Si_3N_4-on-SOI integrated photonics platform *Opt. Express* **22** 11167
[17] Blumenthal D J, Heideman R, Geuzebroek D, Leinse A and Roeloffzen C 2018 Silicon nitride in silicon photonics *Proc. IEEE* **106** 2209–31
[18] Bose D, Harrington M W, Isichenko A, Liu K, Wang J, Chauhan N, Newman Z L and Blumenthal D J 2024 Anneal-free ultra-low loss silicon nitride integrated photonics *Light Sci. Appl.* **13** 156
[19] Sharma T, Wang J, Kaushik B K, Cheng Z, Kumar R, Wei Z and Li X 2020 Review of recent progress on silicon nitride-based photonic integrated circuits *IEEE Access* **8** 195436–46
[20] Xiang C, Jin W and Bowers J E 2022 Silicon nitride passive and active photonic integrated circuits: trends and prospects *Photonics Res.* **10** A82–A96
[21] Guzman R C D, Yang J, Cheng M M C, Salley S O and Ng K Y S 2014 High capacity silicon nitride-based composite anodes for lithium ion batteries *J. Mater. Chem. A* **2** 14577–84
[22] Wu C Y, Chang C C and Duh J G 2016 Silicon nitride coated silicon thin film on three dimensions current collector for lithium ion battery anode *J. Power Sources* **325** 64–70
[23] Ulvestad A, Andersen H F, J P, Prytz O and Kirkengen M 2017 Long-term cyclability of substoichiometric silicon nitride thin film anodes for Li-ion batteries *Sci. Rep.* **7** 13315
[24] Ulvestad A, Andersen H F, Jensen I J T, Mongstad T T, Mæhlen J P and Kirkengen M 2018 Substoichiometric silicon nitride – an anode material for Li-ion batteries promising high stability and high capacity *Sci. Rep.* **8** 8634
[25] Ulvestad A J P and Kirkengen M 2018 Silicon nitride as anode material for li-ion batteries: understanding the SiN_x conversion reaction *J. Power Sources* **399** 414–21
[26] Huang X D, Gan X F, Zhang F, Huang Q A and Yang J Z 2018 Improved electrochemical performance of silicon nitride film by hydrogen incorporation for lithium-ion battery anode *Electrochim. Acta* **268** 241–47
[27] Ulvestad A et al 2021 Stoichiometry-controlled reversible lithiation capacity in nanostructured silicon nitrides enabled by in situ conversion reaction *ACS Nano* **15** 16777–87
[28] Lovett A J, Füredi M, Bird L, Said S, Frost B, Shearing P R, Guldin S and Miller T S 2025 Structural evolution of silicon nitride anodes during electrochemical lithiation *ACS Electrochem.* **1** 962–73
[29] Nemaga A W, Lai S Y, Nguyen T, Ulvestad A and Foss C E L 2025 Unveiling the advantages of silicon nitride nanoparticle anodes for enhanced cyclic stability, rate performance and mechanical robustness *ACS Omega* **10** 2608–15
[30] Cottom J, Hückmann L, Meyer J and Olsson E 2025 Forged by charge: polaron-induced matrix formation in silicon nitride conversion-type anodes for lithium-ion batteries *J. Mater. Chem. A* **13** 34260–72
[31] Villanueva L G and Schmid S 2014 Evidence of surface loss as ubiquitous limiting damping mechanism in SiN micro- and nanomechanical resonators *Phys. Rev. Lett.* **113** 227201
[32] Bereyhi M J, Arabmoheghi A, Beccari A, Fedorov S A, Huang G, Kippenberg T J and Engelsen N J 2022 Perimeter modes of nanomechanical resonators exhibit quality factors exceeding 10^9 at room temperature *Phys. Rev. X* **12** 021036
[33] Cupertino A, Shin D, Guo L, Steeneken P G, Bessa M A and Norte R A 2024 Centimeter-scale nanomechanical resonators with low dissipation *Nat. Commun.* **15** 4255
[34] Lu C Y 2012 Future prospects of NAND flash memory technology–the evolution from floating gate to charge trapping to 3D stacking *J. Nanosci. Nanotechnol.* **12** 7604–18
[35] Spassov D and Paskaleva A 2023 Challenges to optimize charge trapping non-volatile flash memory cells: A case study of HfO_2/Al_2O_3 nanolaminated stacks *Nanomaterials* **13** 2456
[36] Kim T H, Park I H, Lee J D, Shin H C and Park B G 2006 Electron trap density distribution of Si-rich silicon nitride extracted using the modified negative charge decay model of silicon-oxide-nitride-oxide-silicon structure at elevated temperatures *Appl. Phys. Lett.* **89** 063508
[37] Suhane A, Arreghini A, Degraeve R, Van den bosch G, Breuil L, Zahid M B, Jurczak M, De Meyer K and Van Houdt J 2010 Validation of retention modeling as a trap-profiling technique for SiN-based charge-trapping memories *IEEE Electron Device Lett.* **31** 77–79
[38] You J H, Kim H W, Kim D H, Kim T W and Lee K W 2011 Effect of the trap density and distribution of the silicon nitride layer on the retention characteristics of charge trap flash memory devices *2011 Int. Conf. on Simulation of Semiconductor Processes and Devices* pp 199–202
[39] Kang H J, Choi N, Joe S M, Seo J H, Choi E, Park S K, Park B G and Lee J H 2015 Comprehensive analysis of retention characteristics in 3-D NAND flash memory cells with tube-type poly-Si channel structure *2015 Symp. on VLSI Technology (VLSI Technology)* pp T182–3
[40] Nam K R, Jeong J K, Sung J Y and Lee G W 2021 Modeling and verification of interface and bulk trap level density extraction in SONOS memory charge trapping layer *Trans. Electr. Electron. Mater.* **22** 372–77
[41] Nam K et al 2022 Optimal energetic-trap distribution of nano-scaled charge trap nitride for wider V_{th} window in 3D NAND flash using a machine-learning method *Nanomaterials* **12** 1808

[42] Son H, Sim K, Hwang H C and Park H 2025 Temperature-induced interfacial intermixing and trap modulation in ONO-based flash memory capacitors *Nanotechnology* **36** 405201
[43] Shaposhnikov A V, Petrov I P, Gritsenko V A and Kim C W 2007 Electronic band structure and effective masses of electrons and holes in the α and β phases of silicon nitride *Phys. Solid State* **49** 1628–32
[44] Lina S H, Chin A, Yeh F S and McAlister S P 2008 Good 150 °C retention and fast erase characteristics in charge-trap-engineered memory having a scaled layer *2008 IEEE Int. Electron Devices Meeting* (https://doi.org/10.1109/IEDM.2008.4796829)
[45] Gismatulin A A, Kamaev G N, Kruchinin V N, Gritsenko V A, Orlov O M and Chin A 2021 Charge transport mechanism in the forming-free memristor based on silicon nitride *Sci. Rep.* **11** 2417
[46] Vedula R P, Anderson N L and Strachan A 2012 Effect of topological disorder on structural, mechanical and electronic properties of amorphous silicon nitride: an atomistic study *Phys. Rev. B* **85** 205209
[47] Hintzsche L E, Fang C M, Watts T, Marsman M, Jordan G, Lamers M W P E, Weeber A W and Kresse G 2012 Density functional theory study of the structural and electronic properties of amorphous silicon nitrides: $Si_3N_{4-x}H_y$ *Phys. Rev. B* **86** 235204
[48] Vedula R P, Palit S, Alam M A and Strachan A 2013 Role of atomic variability in dielectric charging: A first-principles-based multiscale modeling study *Phys. Rev. B* **88** 205204
[49] Hintzsche L E, Fang C M, Marsman M, Jordan G, Lamers M W P E, Weeber A W and Kresse G 2013 Defects and defect healing in amorphous $Si_3N_4 - xH_y$: an ab initio density functional theory study *Phys. Rev. B* **88** 155204
[50] Kang G, Lee D, Lee K, Kim J and Han S 2018 First-principles study on the negative-*U* behavior of *K* centers in amorphous $Si_3N_4 - x$ *Phys. Rev. Appl.* **10** 064052
[51] Wilhelmer C, Waldhoer D, Milardovich D, Cvitkovich L, Waltl M and Grasser T 2023 Intrinsic electron trapping in amorphous silicon nitride (a-Si_3N_4:H) *2023 Int. Conf. on Simulation of Semiconductor Processes and Devices (SISPAD)* pp 149–52
[52] Wilhelmer C, Waldhör D, Cvitkovich L, Milardovich D, Waltl M and Grasser T 2024 Polaron formation in the hydrogenated amorphous silicon nitride Si_3N_4 : H *Phys. Rev. B* **110** 045201
[53] Hückmann L, Cottom J and Meyer J 2024 Intrinsic charge trapping and reversible charge induced structural modifications in a-Si_3N_4 *Adv. Phys. Res.* **3** 2300109
[54] Cottom J, Hückmann L, Olsson E and Meyer J 2024 From Jekyll to Hyde and beyond: hydrogen's multifaceted role in passivation, H-induced breakdown and charging of amorphous silicon nitride *J. Phys. Chem. Lett.* **15** 840–48
[55] Choi W I, Son W J, Dronskowski R, Oh Y, Yang S Y, Kwon U and Kim D S 2024 Switchable chemical-bond reorganization for the stable charge trapping in amorphous silicon nitride *Adv. Mater.* **36** 2308054
[56] Boero M, Shiraishi K, Nagahashi T, Nanataki F and Oshiyama A 2025 Space-induced floating electronic states in non-stoichiometric amorphous silicon nitride for memory devices applications *Phys. Rev. Mater.* **9** 084601
[57] Choi W I, Kim B, Kwon U, Cho Y H, Son W J, Jeong H, Dronskowski R and Kim D S 2025 Anderson's negative-*U* chemistry in amorphous silicon nitride: a complex system approach *Sci. Adv.* **11** eadx9540
[58] Nagahashi T, Oshiyama A, Boero M, Karasawa H, Horiike R and Shiraishi K 2025 Silicon-richness impact for enhanced charge-trapping in 3D NAND flash memories *IEEE J. Electron Devices Soc.* **7** 1756–1763
[59] El-Sayed A M, Watkins M B, Afanas'ev V V and Shluger A L 2014 Nature of intrinsic and extrinsic electron trapping in SiO_2 *Phys. Rev. B* **89** 125201
[60] Wilhelmer C, Waldhoer D, Jech M, El-Sayed A M B, Cvitkovich L, Waltl M and Grasser T 2022 Ab initio investigations in amorphous silicon dioxide: proposing a multi-state defect model for electron and hole capture *Microelectron. Reliab.* **139** 114801
[61] Aiyama T, Fukunaga T, Niihara K, Hirai T and Suzuki K 1979 An x-ray diffraction study of the amorphous structure of chemically vapor-deposited silicon nitride *J. Non-Cryst. Solids* **33** 131–39
[62] Hückmann L, Sylvia R, Blankenvoorde F, Cottom J and Meyer J 2026 Mechanistic insights into the dry oxidation of amorphous silicon nitride: A DFT study *J. Mater. Chem. C* **14** 139–51
[63] Ahn H, Park H S, Gu M, Khim Y H, Kim H D, Im J, Nam S, Choi E, Chang Y J and Han M 2025 Ti-doping in silicon nitride: enhanced charge trap characteristics for flash memory *ACS Appl. Electron. Mater.* **7** 1756–63
[64] Gritsenko V A, Perevalov T V, Novikov Y N and Gismatulin A A 2026 Boron-irradiated Si_3N_4: the origin of the defect responsible for the red shift of fundamental absorption edge and increase of refractive index *Appl. Surf. Sci.* **724** 165776
[65] Wilhelmer C, Waldhoer D, Cvitkovich L, Milardovich D, Waltl M and Grasser T 2023 Over- and undercoordinated atoms as a source of electron and hole traps in amorphous silicon nitride (a-Si_3N_4) *Nanomaterials* **13** 2286
[66] Gritsenko V A, Nekrashevich S S, Vasilev V V and Shaposhnikov A V 2009 Electronic structure of memory traps in silicon nitride *Microelectron. Eng.* **86** 1866–69
[67] Gritsenko V A, Perevalov T V, Orlov O M and Krasnikov G Y 2016 Nature of traps responsible for the memory effect in silicon nitride *Appl. Phys. Lett.* **109** 4959830
[68] Alkauskas A, Lyons J L, Steiauf D and Van de Walle C G 2012 First-principles calculations of luminescence spectrum line shapes for defects in semiconductors: the example of GaN and ZnO *Phys. Rev. Lett.* **109** 267401
[69] Alkauskas A, Yan Q and Van de Walle C G 2014 First-principles theory of nonradiative carrier capture via multiphonon emission *Phys. Rev. B* **90** 075202
[70] Goes W, Wimmer Y, El-Sayed A M, Rzepa G, Jech M, Shluger A L and Grasser T 2018 Identification of oxide defects in semiconductor devices: A systematic approach linking DFT to rate equations and experimental evidence *Microelectron. Reliab.* **87** 286–320
[71] Grasser T 2012 Stochastic charge trapping in oxides: from random telegraph noise to bias temperature instabilities *Microelectron. Reliab.* **52** 39–70
[72] Waldhoer D *et al* 2023 Comphy v3.0—A compact-physics framework for modeling charge trapping related reliability phenomena in MOS devices *Microelectron. Reliab.* **146** 115004
[73] Karl A *et al* 2025 A standardized approach to characterize hysteresis in 2D-materials-based transistors for stability benchmarking and performance projection *Nat. Commun.* **17** 171
[74] Kim K and Lee S Y 2007 Memory technology in the future *Microelectron. Eng.* **84** 1976–81
[75] Choi H and Shin H 2025 A compact model for program operation of gate-all-around barrier-engineered charge-trapping NAND flash memory in the FN-tunneling regime *IEEE J. Electron Devices Soc.* **13** 1237–42
[76] Lue H T *et al* 2010 A highly scalable 8-layer 3D vertical-gate (VG) TFT NAND flash using junction-free buried channel BE-SONOS device *2010 Symp. on VLSI Technology* pp 131–32
[77] Oh Y T, Sim J M, Kino H, Kim D K, Tanaka T and Song Y H 2019 The effect of tungsten volume on residual stress and cell characteristics in MONOS *IEEE J. Electron Devices Soc.* **7** 382–87

[78] Schanovsky F, Verreck D, Stanojević Z, Schallert S, Arreghini A, van den Bosch G, Rosmeulen M and Karner M 2024 Modeling the operation of charge trap flash memory–Part I: the importance of carrier energy relaxation *IEEE Trans. Electron Devicess* **71** 547–53

[79] Arreghini A, Akil N, Driussi F, Esseni D, Selmi L and Duuren M J V 2008 Long term charge retention dynamics of SONOS cells *Solid-State Electron.* **52** 1460–66

[80] Ravindra N M and Zhao J 1992 Fowler-Nordheim tunneling in thin SiO_2 films *Smart Mater. Struct.* **1** 197

[81] Hwang J, Park M K, Cho J, Yang Y, Bae J H and Lee J H 2025 Nearly temperature-independent gate-electric-field-driven lateral migration of electrons in Si_3N_4 charge trap layer of flash memory devices *Phys. Rev. Lett.* **135** 157001

[82] Liu Y Y, Liu F, Wang R, Luo J W, Jiang X, Huang R, Li S S and Wang L W 2019 Characterizing the charge trapping across crystalline and amorphous $Si/SiO_2/HfO_2$ stacks from first-principle calculations *Phys. Rev. Appl.* **12** 064012

[83] Verreck D *et al* 2021 Understanding the ISPP slope in charge trap flash memory and its impact on 3-D NAND scaling *2021 IEEE Int. Electron Devices Meeting (IEDM)* pp 1–4

[84] Arreghini A, Driussi F, Vianello E, Esseni D, van Duuren M J, Golubovic D S, Akil N and van Schaijk R 2008 Experimental characterization of the vertical position of the trapped charge in si nitride-based nonvolatile memory cells *IEEE Trans. Electron Devices* **55** 1211–19

[85] Degraeve R, Cho M, Govoreanu B, Kaczer B, Zahid M B, Van Houdt J, Jurczak M and Groeseneken G 2008 Trap spectroscopy by charge injection and sensing (TSCIS): a quantitative electrical technique for studying defects in dielectric stacks *2008 IEEE Int. Electron Devices Meeting* (https://doi.org/10.1109/IEDM.2008.4796812)

[86] Wang Y and White M H 2005 An analytical retention model for SONOS nonvolatile memory devices in the excess electron state *Solid-State Electron.* **49** 97–107

[87] Woo C, Kim S, Park J, Lee D, Kang M, Jeon J and Shin H 2019 Modeling of lateral migration mechanism during the retention operation in 3D NAND flash memories *2019 Electron Devices Technology and Manufacturing Conf. (EDTM)* pp 261–63

[88] Han I and Shin H 2026 Machine learning-based investigation of temperature effects on lateral migration in 3-D nand flash memory *IEEE Trans. Electron Devices* **73** 2747–53

[89] Yoo H N, Choi B, Back J W, Kang H J, Kwon E, Chung S, Bae J H, Park B G and Lee J H 2021 Effect of lateral charge diffusion on retention characteristics of 3D NAND flash cells *IEEE Electron Device Lett.* **42** 1148–51

[90] Hwang J, Bae J H, Park M K and Lee J H 2026 Direct observation of lateral hole migration in the charge trap layer of an inhomogeneous flash memory device *Appl. Phys. Rev.* **13** 011424

[91] Bachhofer H, Reisinger H, Bertagnolli E and von Philipsborn H 2001 Transient conduction in multidielectric silicon–oxide–nitride–oxide semiconductor structures *J. Appl. Phys.* **89** 2791–800

[92] Lai S C *et al* 2007 A study on the erase and retention mechanisms for MONOS, MANOS and BE-SONOS non-volatile memory devices *VLSI-TSA* pp 1–2

[93] Kim D H *et al* 2010 Program/Erase model of nitride-based NAND-type charge trap flash memories *Jpn. J. Appl. Phys.* **49** 084301

[94] Kim D H, Park S, Seo Y, Kim T, Kim D M and Cho I 2012 Comparative investigation of endurance and bias temperature instability characteristics in metal-Al_2O_3-nitride-oxide-semiconductor (MANOS) and semiconductor-oxide-nitride-oxide-semiconductor (SONOS) charge trap flash memory *J. Semicond. Technol. Sci.* **12** 449

[95] Wang C M, Pan X, Rühle M, Riley F L and Mitomo M 1996 Silicon nitride crystal structure and observations of lattice defects *J. Mater. Sci.* **31** 5281–98

[96] Du Boulay D, Ishizawa N, Atake T, Streltsov V, Furuya K and Munakata F 2004 Synchrotron x-ray and ab initio studies of β-Si_3N_4 *Acta Crystallogr. B* **60** 388–405

[97] Jiang J Z K, Berg R W, Frost D J, Zhou T J and Shi P X 2000 Structural characterization of cubic silicon nitride *Europhys. Lett.* **51** 62

[98] Zerr A, Miehe G, Serghiou G, Schwarz M, Kroke E, Riedel R, Fue H, Kroll P and Boehler R 1999 Synthesis of cubic silicon nitride *Nature* **400** 340–42

[99] Chu T L, Lee C H and Gruber G A 1967 The preparation and properties of amorphous silicon nitride films *J. Electrochem. Soc.* **114** 717

[100] Yeheskel O and Gefen Y 1985 The effect of the α phase on the elastic properties of Si_3N_4 *Mater. Sci. Eng.* **71** 95–99

[101] Vogelgesang R, Grimsditch M and Wallace J S 2000 The elastic constants of single crystal β-Si_3N_4 *Appl. Phys. Lett.* **76** 982–84

[102] Zerr A, Kempf M, Schwarz M, Kroke E, Göken M and Riedel R 2002 Elastic moduli and hardness of cubic silicon nitride *J. Am. Ceram. Soc.* **85** 86–90

[103] Khan A, Philip J and Hess P 2004 Young's modulus of silicon nitride used in scanning force microscope cantilevers *J. Appl. Phys.* **95** 1667–72

[104] Zhang L, Jin H, Yang W, Xie Z, Miao H and An L 2005 Optical properties of single-crystalline α-Si_3N_4 nanobelts *Appl. Phys. Lett.* **86** 061908

[105] Wu C L, Chen W S and Su Y H 2012 N_2-plasma nitridation on Si(111): its effect on crystalline silicon nitride growth *Surf. Sci.* **606** L51–L54

[106] Museur L, Zerr A and Kanaev A 2016 Photoluminescence and electronic transitions in cubic silicon nitride *Sci. Rep.* **6** 18523

[107] Resende J, Fuard D, Le Cunff D, Tortai J H and Pelissier B 2021 Hybridization of ellipsometry and energy loss spectra from XPS for bandgap and optical constants determination in SiON thin films *Mater. Chem. Phys.* **259** 124000

[108] Singh P, Harbola M K and Johnson D D 2017 Better band gaps for wide-gap semiconductors from a locally corrected exchange-correlation potential that nearly eliminates self-interaction errors *J. Phys.: Condens. Matter* **29** 424001

[109] Huang Z, Chen F, Su R, Wang Z, Li J, Shen Q and Zhang L 2015 Electronic and optical properties of Y-doped Si_3N_4 by density functional theory *J. Alloys Compd.* **637** 376–81

[110] Kresse G, Marsman M, Hintzsche L E and Flage-Larsen E 2012 Optical and electronic properties of Si_3N_4 and α-SiO_2 *Phys. Rev. B* **85** 045205

[111] Han Y X, Yang C L, Xiao K L, Wang L Z, Wang M S and Ma X G 2014 Energy gap tuning and optical properties of γ-Si_3N_4 doped with Fe, Co and Ni *Mater. Sci. Semicond. Process.* **27** 474–81

[112] Huang Z, Chen F, Shen Q and Zhang L 2016 Linking photoluminescence of α-Si_3N_4 to intrinsic point defects via band structure modelling *RSC Adv.* **6** 7568–74

[113] Wu J, Chen J and Jiang X 2019 Multiscale simulation of lateral charge loss in Si_3N_4 3D NAND flash based on density functional theory *J. Phys. D: Appl. Phys.* **52** 395103

[114] Mohn C E H, Vajeeston P, Valldor M and Bergum K 2026 Benchmarking density functional theory for accurate calculation of nitride band gaps *J. Chem. Theory Comput.* **22** 1321–37

[115] Ren S Y and Ching W Y 1981 Electronic structures of β- and α-silicon nitride *Phys. Rev. B* **23** 5454–63
[116] Tsai *et al* 2016 Approaching defect-free amorphous silicon nitride by plasma-assisted atomic beam deposition for high performance gate dielectric *Sci. Rep.* **6** 28326
[117] Xiao H, Tahir-Kheli J and Goddard W A I 2011 Accurate band gaps for semiconductors from density functional theory *J. Phys. Chem. Lett.* **2** 212–17
[118] Priest H F, Burns F C, Priest G L and Skaar E C 1973 Oxygen content of alpha silicon nitride *J. Am. Ceram. Soc.* **56** 395–395
[119] Goodman P and O'Keeffe M 1980 The space group of β-Si_3N_4 *Acta Crystallogr. B* **36** 2891–93
[120] Messier D R, Riley F L and Brook R J 1978 The α/β silicon nitride phase transformation *J. Mater. Sci.* **13** 1199–205
[121] Liang J J, Topor L, Navrotsky A and Mitomo M 1999 Silicon nitride: enthalpy of formation of the α- and β-polymorphs and the effect of C and O impurities *J. Mater. Res.* **14** 1959–68
[122] Jiang J Z, Kragh F, Frost D J, Stahl K and Lindelov H 2001 Hardness and thermal stability of cubic silicon nitride *J. Phys.: Condens. Matter* **13** L515
[123] Pacchioni G and Erbetta D 2000 Charge transfer and charge conversion of *K* and *N* defect centers in Si_3N_4 *Phys. Rev. B* **61** 15005–10
[124] Gritsenko V A, Novikov Y N, Shaposhnikov A V and Morokov Y N 2001 Numerical simulation of intrinsic defects in SiO_2 and Si_3N_4 *Semiconductors* **35** 997–1005
[125] Petersen M and Roizin Y 2006 Density functional theory study of deep traps in silicon nitride memories *Appl. Phys. Lett.* **89** 053511
[126] Di Valentin C, Palma G and Pacchioni G 2011 Ab initio study of transition levels for intrinsic defects in silicon nitride *J. Phys. Chem C* **115** 561–69
[127] Vianello E, Driussi F, Blaise P, Palestri P, Esseni D, Perniola L, Molas G, De Salvo B and Selmi L 2011 Explanation of the charge trapping properties of silicon nitride storage layers for NVMs—Part II: atomistic and electrical modeling *IEEE Trans. Electron Devices* **58** 2490–99
[128] Wang X S 1999 Crystalline Si_3N_4 thin films on Si(111) and the 4×4 reconstruction on Si_3N_4(0001) *Phys. Rev. B* **60** R2146–9
[129] Raju K, Moon S, Kim M, Cho J and Lee H K 2025 Catalyst-free synthesis of Si_3N_4 powders via direct nitridation of Si: influence of particle size and nitridation parameters on the α-phase fraction *J. Korean Ceram. Soc.* **62** 656–65
[130] Becher P F *et al* 1998 Microstructural design of silicon nitride with improved fracture toughness: I, effects of grain shape and size *J. Am. Ceram. Soc.* **81** 2821–30
[131] Wang C M, Pan X, Hoffmann M J, Cannon R M and Riihle M 1996 Grain boundary films in rare-earth-glass-based silicon nitride *J. Am. Ceram. Soc.* **79** 788–92
[132] Hampshire S and Pomeroy M J 2012 Grain boundary glasses in silicon nitride: a review of chemistry, properties and crystallisation *J. Eur. Ceram. Soc.* **32** 1925–32
[133] Roenigk K F and Jensen K F 1987 Low pressure CVD of silicon nitride *J. Electrochem. Soc.* **134** 1777
[134] Karouta F, Vora K, Tian J and Jagadish C 2012 Structural, compositional and optical properties of PECVD silicon nitride layers *J. Phys. D: Appl. Phys.* **45** 445301
[135] Yang C and Pham J 2018 Characteristic study of silicon nitride films deposited by LPCVD and PECVD *Silicon* **10** 2561–67
[136] Cossou B, Jacques S, Couégnat G, King S W, Li L, Lanford W A, Bhattarai G, Paquette M and Chollon G 2019 Synthesis and optimization of low-pressure chemical vapor deposition-silicon nitride coatings deposited from $SiHCl_3$ and NH_3 *Thin Solid Films* **681** 47–57
[137] Goto H, Shibahara K and Yokoyama S 1996 Atomic layer controlled deposition of silicon nitride with self limiting mechanism *Appl. Phys. Lett.* **68** 3257–59
[138] Klaus J W, Ott A W, Dillon A C and George S M 1998 Atomic layer controlled growth of Si_3N_4 films using sequential surface reactions *Surf. Sci.* **418** L14–L19
[139] Nagata K, Nagasaka M, Yamaguchi T, Ogura A, Oji H, Son J Y, Hirosawa I, Watanabe Y and Hirota Y 2013 Evaluation of stress induced by plasma assisted ALD SiN film *ECS Trans.* **53** 51
[140] Kim H, Song H, Shin C, Kim K, Jang W, Kim H, Shin S and Jeon H 2016 Dielectric barrier characteristics of Si-rich silicon nitride films deposited by plasma enhanced atomic layer deposition *J. Vac. Sci. Technol. A* **35** 01A101
[141] Oh S J, Ma B S, Yang C and Kim T S 2022 Intrinsic mechanical properties of free-standing SiN_x thin films depending on PECVD conditions for controlling residual stress *ACS Appl. Electron. Mater.* **4** 3980–87
[142] Ovanesyan R A, Hausmann D M and Agarwal S 2018 A three-step atomic layer deposition process for SiN_x using Si_2Cl_6, CH_3NH_2 and N_2 plasma *ACS Appl. Mater. Interfaces* **10** 19153–61
[143] Kaloyeros A E, Pan Y, Goff J and Arkles B 2020 Review—Silicon nitride and silicon nitride-rich thin film technologies: state-of-the-art processing technologies, properties and applications *ECS J. Solid State Sci. Technol.* **9** 063006
[144] Hu S M and Gregor L V 1967 Silicon nitride films by reactive sputtering *J. Electrochem. Soc.* **114** 826
[145] Signore M A, Sytchkova A, Dimaio D, Cappello A and Rizzo A 2012 Deposition of silicon nitride thin films by RF magnetron sputtering: A material and growth process study *Opt. Mater.* **34** 632–38
[146] Kiseleva D V, Yurjev Y N, Petrakov Y V, Sidelev D V, Korzhenko D V and Erofeev E V 2017 Study on the influence of the magnetron power supply on the properties of the silicon nitride films *J. Phys.: Conf. Ser.* 789 012028
[147] Dergez D, Schneider M, Bittner A, Pawlak N and Schmid U 2016 Mechanical and electrical properties of RF magnetron sputter deposited amorphous silicon-rich silicon nitride thin films *Thin Solid Films* **606** 7–12
[148] Hirohata Y, Shimamoto N, Hino T, Yamashima T and Yabe K 1994 Properties of silicon nitride films prepared by magnetron sputtering *Thin Solid Films* **253** 425–29
[149] Kaloyeros A E, Jové F A, Goff J and Arkles B 2017 Review—Silicon nitride and silicon nitride-rich thin film technologies: trends in deposition techniques and related applications *ECS J. Solid State Sci. Technol.* **6** 691
[150] Pandey R K, Patil L S, Bange J P and Gautam D K 2004 Growth and characterization of silicon nitride films for optoelectronics applications *Opt. Mater.* **27** 139–46
[151] Keita A S, En Naciri A, Delachat F, Carrada M, Ferblantier G, Slaoui A and Stchakovsky M 2011 Dielectric functions of PECVD-grown silicon nanoscale inclusions within rapid thermal annealed silicon-rich silicon nitride films *Thin Solid Films* **519** 2870–73
[152] Gyulai J, Meyer O, Mayer J W and Rodriguez V 1970 Analysis of silicon nitride layers on silicon by backscattering and channeling effect measurements *Appl. Phys. Lett.* **16** 232–34
[153] Nguyen S V and Fridmann S 1987 Plasma deposition and characterization of thin silicon rich silicon nitride films *J. Electrochem. Soc.* **134** 2324

[154] Custer J S, Thompson M O, Jacobson D C, Poate J M, Roorda S, Sinke W C and Spaepen F 1994 Density of amorphous Si *Appl. Phys. Lett.* **64** 437–39
[155] Deshpande S V, Gulari E, Brown S W and Rand S C 1995 Optical properties of silicon nitride films deposited by hot filament chemical vapor deposition *J. Appl. Phys.* **77** 6534–41
[156] Iqbal A, Jackson W B, Tsai C C, Allen J W and Bates J C W 1987 Electronic structure of silicon nitride and amorphous silicon/silicon nitride band offsets by electron spectroscopy *J. Appl. Phys.* **61** 2947–54
[157] Gritsenko V A, Kruchinin V N, Prosvirin I P, Novikov Y N, Chin A and Volodin V A 2019 Atomic and electronic structures of a-SiN_x:H *J. Exp. Theor. Phys.* **129** 924–34
[158] Futako W, Kamiya T, Fortmann C M and Shimizu I 2000 The structure of 1.5–2.0 eV band gap amorphous silicon films prepared by chemical annealing *J. Non-Cryst. Solids* **266–269** 630–34
[159] Roizin Y 1991 Failure phenomena due to hydrogen migration in amorphous a-SiN_x:H films *J. Non-Cryst. Solids* **137–138** 61–64
[160] Martínez F L, del Prado A, Mártil I, González-Díaz G, Selle B and Sieber I 1999 Thermally induced changes in the optical properties of SiN_x:H films deposited by the electron cyclotron resonance plasma method *J. Appl. Phys.* **86** 2055–61
[161] Reynes B and Bruyère J C 1992 PECVD silicon nitrides with low hydrogen content *Sens. Act. A* **33** 25–28
[162] Santana G, Fandiño J, Ortiz A and Alonso J C 2005 Low temperature–low hydrogen content silicon nitrides thin films deposited by PECVD using dichlorosilane and ammonia mixtures *J. Non-Cryst. Solids* **351** 922–28
[163] Ovanesyan R A, Hausmann D M and Agarwal S 2015 Low-temperature conformal atomic layer deposition of SiN_x films using Si_2Cl_6 and NH_3 plasma *ACS Appl. Mater. Interfaces* **7** 10806–13
[164] Stein H J and Wegener H A R 1977 Chemically bound hydrogen in CVD Si_3N_4: dependence on NH_3/SiH_4 ratio and on annealing *J. Electrochem. Soc.* **124** 908
[165] Misawa M, Fukunaga T, Niihara K, Hirai T and Suzuki K 1979 Structure characterization of CVD amorphous Si_3N_4 by pulsed neutron total scattering *J. Non-Cryst. Solids* **34** 313–21
[166] Wakita K W K, Hayashi H H H and Nakayama Y N Y 1996 Structural study of amorphous SiN_x:H films produced by plasma-enhanced chemical vapor deposition *Jpn. J. Appl. Phys.* **35** 2557
[167] Zachariasen W H 1932 The atomic arrangement in glass *J. Am. Chem. Soc.* **54** 3841–51
[168] Robertson J and Powell M J 1984 Gap states in silicon nitride *Appl. Phys. Lett.* **44** 415–17
[169] Robertson J 1991 Electronic structure of silicon nitride *Phil. Mag. B* **63** 47–77
[170] Robertson J 1994 Defects and hydrogen in amorphous silicon nitride *Philos. Mag. B* **69** 307–26
[171] Warren W L, Kanicki J, Robertson J, Poindexter E H and McWhorter P J 1993 Electron paramagnetic resonance investigation of charge trapping centers in amorphous silicon nitride films *J. Appl. Phys.* **74** 4034–46
[172] Robertson J, Warren W L and Kanicki J 1995 Nature of the Si and N dangling bonds in silicon nitride *J. Non-Cryst. Solids* **187** 297–300
[173] Delachat F, Carrada M, Ferblantier G, Grob J J and Slaoui A 2009 Properties of silicon nanoparticles embedded in SiN_x deposited by microwave-PECVD *Nanotechnology* **20** 415608
[174] Torchynska T V, Casas Espinola J L, Vergara Hernandez E, Khomenkova L, Delachat F and Slaoui A 2015 Effect of the stoichiometry of Si-rich silicon nitride thin films on their photoluminescence and structural properties *Thin Solid Films* **581** 65–69
[175] Kob W 1999 Computer simulations of supercooled liquids and glasses *J. Phys.: Condens. Matter* **11** R85
[176] Strand J, Kaviani M, Gao D, El-Sayed A M, Afanas'ev V V and Shluger A L 2018 Intrinsic charge trapping in amorphous oxide films: status and challenges *J. Phys.: Condens. Matter* **30** 233001
[177] Liu H, Zhao Z, Zhou Q, Chen R, Yang K, Wang Z, Tang L and Bauchy M 2022 Challenges and opportunities in atomistic simulations of glasses: a review *C. R.-Geosci.* **354** 35–77
[178] Christie J K 2023 Review: understanding the properties of amorphous materials with high-performance computing methods *Philos. Trans. R. Soc. A* **381** 20220251
[179] Drabold D A 2009 Topics in the theory of amorphous materials *Eur. Phys. J. B* **68** 1–21
[180] Li X, Song W, Yang K, Krishnan N M A, Wang B, Smedskjaer M M, Mauro J C, Sant G, Balonis M and Bauchy M 2017 Cooling rate effects in sodium silicate glasses: bridging the gap between molecular dynamics simulations and experiments *J. Chem. Phys.* **147** 074501
[181] Debenedetti P G and Stillinger F H 2001 Supercooled liquids and the glass transition *Nature* **410** 259–67
[182] Vollmayr K, Kob W and Binder K 1996 How do the properties of a glass depend on the cooling rate? A computer simulation study of a Lennard Jones system *J. Chem. Phys.* **105** 4714–28
[183] Liu Z, Hu Y, Li X, Song W, Goyal S, Micoulaut M and Bauchy M 2018 Glass relaxation and hysteresis of the glass transition by molecular dynamics simulations *Phys. Rev. B* **98** 104205
[184] Vollmayr K, Kob W and Binder K 1996 Cooling-rate effects in amorphous silica: A computer-simulation study *Phys. Rev. B* **54** 15808–27
[185] Lane J M D 2015 Cooling rate and stress relaxation in silica melts and glasses via microsecond molecular dynamics *Phys. Rev. E* **92** 012320
[186] de Brito Mota F, Justo J F and Fazzio A 1998 Structural properties of amorphous silicon nitride *Phys. Rev. B* **58** 8323–28
[187] de Brito Mota F, Justo J F and Fazzio A 1999 Hydrogen role on the properties of amorphous silicon nitride *J. Appl. Phys.* **86** 1843–47
[188] Matsunaga K and Iwamoto Y 2001 Molecular dynamics study of atomic structure and diffusion behavior in amorphous silicon nitride containing boron *J. Am. Ceram. Soc.* **84** 2213–19
[189] Vashishta P, Kalia R K, Nakano A, Li W and Ebbsjö I 1997 Molecular dynamics methods and large-scale simulations of amorphous materials *Amorph. Insul. Semicond.* **20** 151–213
[190] Gastreich M, Gale J D and Marian C M 2003 Charged-particle potential for boron nitrides, silicon nitrides and borosilazane ceramics: derivation of parameters and probing of capabilities *Phys. Rev. B* **68** 094110
[191] Marian C M, Gastreich M and Gale J D 2000 Empirical two-body potential for solid silicon nitride, boron nitride and borosilazane modifications *Phys. Rev. B* **62** 3117–24
[192] Dasmahapatra A and Kroll P 2018 Modeling amorphous silicon nitride: A comparative study of empirical potentials *Comput. Mater. Sci.* **148** 165–75
[193] Milardovich D, Wilhelmer C, Waldhoer D, Cvitkovich L, Sivaraman G and Grasser T 2023 Machine learning interatomic potential for silicon-nitride (Si_3N_4) by active learning *J. Chem. Phys.* **158** 194802

[194] Nayak G K, Srinivasan P, Todt J, Daniel R, Nicolini P and Holec D 2025 Accurate prediction of structural and mechanical properties on amorphous materials enabled through machine-learning potentials: A case study of silicon nitride *Comput. Mater. Sci.* **249** 113629
[195] Yu D, Zhu L, Cui X, Ning X, Li J and Liao D 2025 A study of the deep learning potential of silicon nitride materials under high temperatures *J. Electron. Mater.* **54** 7557–72
[196] Madanchi A, Azek E, Zongo K, Béland L K, Mousseau N and Simine L 2025 Is the future of materials amorphous? Challenges and opportunities in simulations of amorphous materials *ACS Phys. Chem. Au* **5** 3–16
[197] Haseen S and Kroll P 2026 A machine-learning interatomic potential for Si-C-N-H with application to polymer-to-ceramic processing of polysilazanes *J. Am. Ceram. Soc.* **109** e70392
[198] Carson R D and Schnatterly S E 1986 Valence-band electronic structure of silicon nitride studied with the use of soft-x-ray emission *Phys. Rev. B* **33** 2432–38
[199] Silvestrelli P L, Marzari N, Vanderbilt D and Parrinello M 1998 Maximally-localized Wannier functions for disordered systems: application to amorphous silicon *Solid State Commun.* **107** 7–11
[200] Urbach F 1953 The long-wavelength edge of photographic sensitivity and of the electronic absorption of solids *Phys. Rev.* **92** 1324–1324
[201] Mott N 1987 The mobility edge since 1967 *J. Phys. C: Solid State Phys.* **20** 3075
[202] Schwartz T, Bartal G, Fishman S and Segev M 2007 Transport and anderson localization in disordered two-dimensional photonic lattices *Nature* **446** 52–55
[203] Billy J, Josse V, Zuo Z, Bernard A, Hambrecht B, Lugan P, Clément D, Sanchez-Palencia L, Bouyer P and Aspect A 2008 Direct observation of anderson localization of matter waves in a controlled disorder *Nature* **453** 891–94
[204] Semeghini G, Landini M, Castilho P, Roy S, Spagnolli G, Trenkwalder A, Fattori M, Inguscio M and Modugno G 2015 Measurement of the mobility edge for 3D anderson localization *Nat. Phys.* **11** 554–59
[205] Pham T A, Li T, Shankar S, Gygi F and Galli G 2011 Microscopic modeling of the dielectric properties of silicon nitride *Phys. Rev. B* **84** 045308
[206] Crowley J M, Tahir-Kheli J and Goddard W A I 2016 Resolution of the band gap prediction problem for materials design *J. Phys. Chem. Lett.* **7** 1198–203
[207] Adamo C and Barone V 1999 Toward reliable density functional methods without adjustable parameters: the PBE0 model *J. Chem. Phys.* **110** 6158–70
[208] Heyd J, Scuseria G E and Ernzerhof M 2003 Hybrid functionals based on a screened Coulomb potential *J. Chem. Phys.* **118** 8207–15
[209] Heyd J and Scuseria G E 2004 Efficient hybrid density functional calculations in solids: assessment of the Heyd–Scuseria–Ernzerhof screened Coulomb hybrid functional *J. Chem. Phys.* **121** 1187–92
[210] Heyd J, Scuseria G E and Ernzerhof M 2006 Erratum: "Hybrid functionals based on a screened Coulomb potential" [J. Chem. Phys. 118, 8207 (2003)] *J. Chem. Phys.* **124** 219906
[211] Krukau A V, Vydrov O A, Izmaylov A F and Scuseria G E 2006 Influence of the exchange screening parameter on the performance of screened hybrid functionals *J. Chem. Phys.* **125** 224106
[212] Shi L and Wang L W 2012 Ab initio calculations of deep-level carrier nonradiative recombination rates in bulk semiconductors *Phys. Rev. Lett.* **109** 245501
[213] Huang K and Rhys A 1950 Theory of light absorption and non-radiative transitions in F-centres *Proc. R. Soc. A* **204** 406–23
[214] Lax M 1952 The Franck Condon principle and its application to crystals *J. Chem. Phys.* **20** 1752–60
[215] Stoneham A M 2001 Non-radiative processes and the interaction of free carriers with defects *Theory Defects Solids: Electron. Struct. Defects Insul. Semicond.* 477–552
[216] Goguenheim D and Lannoo M 1990 Theoretical and experimental aspects of the thermal dependence of electron capture coefficients *J. Appl. Phys.* **68** 1059–69
[217] Alkauskas A, McCluskey M D and Van de Walle C G 2016 Tutorial: defects in semiconductors—Combining experiment and theory *J. Appl. Phys.* **119** 181101
[218] Abakumov V N, Perel V I and Yassievich I N 1991 *Nonradiative Recombination in Semiconductors (Modern Problems in Condensed Matter Sciences)* (North Holland)
[219] Turiansky M E, Alkauskas A, Engel M, Kresse G, Wickramaratne D, Shen J-X, Dreyer C E and Van de Walle C G 2021 Nonrad: computing nonradiative capture coefficients from first principles *Comput. Phys. Commun.* **267** 108056
[220] Michl J *et al* 2021 Efficient modeling of charge trapping at cryogenic Temperatures—Part I: theory *IEEE Trans. Electron Devices* **68** 6365–71
[221] Karl A, Waldhoer D, Knobloch T, Wilhelmer C and Grasser T 2026 Efficient Quantum-Mechanical Modeling of Nonradiative Charge Transfer Processes (https://doi.org/10.48550/arXiv.2607.17730)
[222] Baroni S, de Gironcoli S, Dal Corso A and Giannozzi P 2001 Phonons and related crystal properties from density-functional perturbation theory *Rev. Mod. Phys.* **73** 515–62
[223] Gritsenko V A 2012 Electronic structure of silicon nitride *Phys.-Usp.* **55** 498
[224] Henry C H and Lang D V 1977 Nonradiative capture and recombination by multiphonon emission in GaAs and GaP *Phys. Rev. B* **15** 989–1016
[225] Schmidt H, Wiebe M, Dittes B and Grundmann M 2007 Meyer-neldel rule in ZnO *Appl. Phys. Lett.* **91** 232110
[226] Vasilev A A, Kochkova A I, Polyakov A Y, Romanov A A, Matros N R, Alexanyan L A, Shchemerov I V and Pearton S J 2024 Observation of temperature-dependent capture cross section for main deep-levels in β-Ga_2O_3 *J. Appl. Phys.* **136** 025701
[227] Freysoldt C, Grabowski B, Hickel T, Neugebauer J, Kresse G, Janotti A and Van de Walle C G 2014 First-principles calculations for point defects in solids *Rev. Mod. Phys.* **86** 253–305
[228] Komsa H P, Rantala T T and Pasquarello A 2012 Finite-size supercell correction schemes for charged defect calculations *Phys. Rev. B* **86** 045112
[229] Krick D T, Lenahan P M and Kanicki J 1988 Electrically active point defects in amorphous silicon nitride: an illumination and charge injection study *J. Appl. Phys.* **64** 3558–63
[230] Warren W L, Lenahan P M and Curry S E 1990 First observation of paramagnetic nitrogen dangling-bond centers in silicon nitride *Phys. Rev. Lett.* **65** 207–10
[231] Warren W L and Lenahan P M 1990 Electron-nuclear double-resonance and electron-spin-resonance study of silicon dangling-bond centers in silicon nitride *Phys. Rev. B* **42** 1773–80

[232] Jousse D, Kanicki J and Stathis J H 1989 Observation of multiple silicon dangling bond configurations in silicon nitride *Appl. Phys. Lett.* **54** 1043–45
[233] Warren W L, Kanicki J, Robertson J and Lenahan P M 1991 Energy level of the nitrogen dangling bond in amorphous silicon nitride *Appl. Phys. Lett.* **59** 1699–701
[234] Warren W L, Rong F C, Poindexter E H, Gerardi G J and Kanicki J 1991 Structural identification of the silicon and nitrogen dangling bond centers in amorphous silicon nitride *J. Appl. Phys.* **70** 346–54
[235] Karpushin A A, Sorokin A N and Gritsenko V A 2016 Si–Si bond as a deep trap for electrons and holes in silicon nitride *JETP Lett.* **103** 171–74
[236] Mine T, Fujisaki K, Ishida T, Shimamoto Y, Yamada R and Torii K 2007 Electron trap characteristics of silicon rich silicon nitride thin films *Jpn. J. Appl. Phys.* **46** 3206
[237] Choi S, Yang H, Chang M, Baek S, Hwang H, Jeon S, Kim J and Kim C 2005 Memory characteristics of silicon nitride with silicon nanocrystals as a charge trapping layer of nonvolatile memory devices *Appl. Phys. Lett.* **86** 251901
[238] Sandhya C, Ganguly U, Chattar N, Olsen C, Seutter S M, Date L, Hung R, Vasi J M and Mahapatra S 2009 Effect of SiN on performance and reliability of charge trap flash (CTF) under Fowler–Nordheim tunneling Program/Erase operation *IEEE Electron Device Lett.* **30** 171–73
[239] Novikov Y N and Gritsenko V A 2020 Charge transport mechanism and amphoteric nature of traps in amorphous silicon nitride *J. Non-Cryst. Solids* **544** 120186
[240] Choi H, Yoo J and Shin H 2024 A new physical model for program transients of cylindrical charge-trap-based NAND flash memories *IEEE Trans. Electron Devices* **71** 2386–92
[241] Choi H, Yoo J and Shin H 2026 Modeling and optimization of 3-D bandgap-engineered NAND flash for program operation by multilayer tunneling with trap physics of tunneling nitride *IEEE Trans. Electron Devices* **73** 1840–48
[242] Yang Y and White M H 2000 Charge retention of scaled SONOS nonvolatile memory devices at elevated temperatures *Solid-State Electron.* **44** 949–58
[243] Winslow D and Williams C 2011 Local density of trap states in SiO_2 and Si_3N_4 films studied by single electron tunneling force spectroscopy *J. Appl. Phys.* **110** 114102
[244] Amosov A V, Kulchin Y N, Dvurechenskii A V and Dzyuba V P 2022 Photoluminescence and excitation energy transfer in non-stoichiometric silicon nitride *J. Lumin.* **243** 118615
[245] Kim H D *et al* 2025 Advanced spectroscopic methods for probing in-gap defect states in amorphous SiN_x for charge trap memory applications *Curr. Appl. Phys.* **69** 21–27
[246] Shin G, Park Y, Jeong J, Kim H and Cho B J 2026 Memory window enhancement with germanium-incorporated charge trap layer in flash memory device *IEEE J. Electron Devices Soc.* **14** 122–26
[247] Kim S, Lee S H, Kim Y G, Cho S and Park B G 2016 Highly compact and accurate circuit-level macro modeling of gate-all-around charge-trap flash memory *Jpn. J. Appl. Phys.* **56** 014302
[248] Lee D C and Shin H 2020 Transient program operation model considering distribution of electrons in 3D NAND flash memories *IEICE Electron. Express* **17** 20200335
[249] Wilhelmer C, Turiansky M E, Waldhör D, Cvitkovich L, Van de Walle C G and Grasser T 2025 Optical properties of vacancies in aluminum oxide (α-Al_2O_3) from first principles *Phys. Rev. Mater.* **9** 096202
[250] Kapoor V J, Xu D, Bailey R S and Turi R A 1992 The combined effect of hydrogen and oxygen impurities in the silicon nitride film of MNOS devices *J. Electrochem. Soc.* **139** 915–21
[251] Dougherty T and Xu Y 2018 Properties and characterization of an aluminium–silicon nitride fibre powder metal composite *SN Appl. Sci.* **1** 135
[252] Mäckel H and Lüdemann R 2002 Detailed study of the composition of hydrogenated SiN_x layers for high-quality silicon surface passivation *J. Appl. Phys.* **92** 2602–09
[253] Volpi F, Braccini M, Devos A, Raymond G, Pasturel A and Morin P 2014 Dual mechanical behaviour of hydrogen in stressed silicon nitride thin films *J. Appl. Phys.* **116** 043506
[254] San Andrés E, del Prado A, Martínez F L, Mártil I, Bravo D and López F J 2000 Rapid thermal annealing effects on the structural properties and density of defects in SiO_2 and SiN_x:H films deposited by electron cyclotron resonance *J. Appl. Phys.* **87** 1187–92
[255] Song C, Huang R, Wang X, Guo Y, Song J, Zhang Y and Zheng Z 2011 Effects of hydrogen on photoluminescence properties of a-SiN_x:H films prepared by VHF-PECVD *Appl. Surf. Sci.* **258** 1290–93
[256] Bommali R K, Ghosh S, Vijaya Prakash G, Gao K, Zhou S, Khan S A and Srivastava P 2014 Hydrogen plasma induced modification of photoluminescence from a-SiN_x:H thin films *J. Appl. Phys.* **115** 053525
[257] Kim H D, An H M, Seo Y, Zhang Y, Park J S and Kim T G 2010 Hydrogen passivation effects under negative bias temperature instability stress in metal/silicon-oxide/silicon-nitride/silicon-oxide/silicon capacitors for flash memories *Microelectron. Reliab.* **50** 21–25
[258] Kobayashi K and Kimoto K 2024 Characterization of hydrogen desorption and charge traps in silicon nitride films *2024 Int. Symp. on Semiconductor Manufacturing (ISSM)* (https://doi.org/10.1109/ISSM64832.2024.10874887)
[259] Choi S *et al* 2025 Effect of hydrogen profile in flash memory SiN_x charge trap layer with different silicon to nitrogen ratios *Adv. Electron. Mater.* **11** e00960
[260] Sung J Y, Jeong J K, Ko W S, Byun J H, Lee H D and Lee G W 2021 High pressure deuterium passivation of charge trapping layer for nonvolatile memory applications *Micromachines* **12** 1316
[261] Godet J and Pasquarello A 2005 Ab initio study of charged states of H in amorphous SiO_2 *Microelectron. Eng.* **80** 288–91
[262] El-Sayed A M, Wimmer Y, Goes W, Grasser T, Afanas'ev V V and Shluger A L 2015 Theoretical models of hydrogen-induced defects in amorphous silicon dioxide *Phys. Rev. B* **92** 014107
[263] El-Sayed A M, Watkins M B, Grasser T, Afanas'ev V V and Shluger A L 2015 Hydrogen-induced rupture of strained si-O bonds in amorphous silicon dioxide *Phys. Rev. Lett.* **114** 115503
[264] Wilhelmer C, Jech M, Waldhoer D, El-Sayed A M B, Cvitkovich L and Grasser T 2021 Statistical ab initio analysis of electron trapping oxide defects in the Si/SiO_2 network *ESSDERC 2021* pp 243–46
[265] Wilhelmer C, Waldhoer D, Jech M, El-Sayed A M B, Cvitkovich L, Waltl M and Grasser T 2022 Metastability of negatively charged hydroxyl-E' centers and their potential role in positive bias temperature instabilities *ESSDERC 2022* pp 376–79
[266] Arapkina L V, Stavrovskii D B and Yuryev V A 2026 Relationship between the electron system and the diffusion of hydrogen atoms in Si_3N_4 layers *J. Appl. Phys.* **139** 175101
[267] Suh S, Ryu S W, Cho S, Kim J R, Kim S, Hwang C S and Kim H J 2015 Low-temperature SiON films deposited by plasma-enhanced atomic layer deposition method using activated silicon precursor *J. Vac. Sci. Technol. A* **34** 01A136

[268] Gritsenko V A, Wong H, Xu J B, Kwok R M, Petrenko I P, Zaitsev B A, Morokov Y N and Novikov Y N 1999 Excess silicon at the silicon nitride/thermal oxide interface in oxide–nitride–oxide structures *J. Appl. Phys.* **86** 3234–40
[269] Alayo M I, Pereyra I, Scopel W L and Fantini M C A 2002 On the nitrogen and oxygen incorporation in plasma-enhanced chemical vapor deposition (PECVD) SiO_xN_y films *Thin Solid Films* **402** 154–61
[270] Klanjšek Gunde M and Maček M 2001 Infrared optical constants and dielectric response functions of silicon nitride and oxynitride films *Phys. Status Solidi a* **183** 439–49
[271] Rebib F, Tomasella E, Dubois M, Cellier J, Sauvage T and Jacquet M 2007 SiO_xN_y thin films deposited by reactive sputtering: process study and structural characterisation *Thin Solid Films* **515** 3480–87
[272] Viard J, Beche E, Perarnau D, Berjoan R and Durand J 1997 XPS and FTIR study of silicon oxynitride thin films *J. Eur. Ceram. Soc.* **17** 2025–28
[273] Chourasia A R and Chopra D R 1993 A study of Si_3N_4 by XPS *Surf. Sci. Spectra* **2** 117–22
[274] Peng Xing D, Zhong Zeng H, Xu Zhang W and Li Zhang W 2019 XPS studies of charging effect induced by x-ray irradiation on amorphous SiO_2 thin films *IOP Conf. Ser.: Mater. Sci. Eng.* **490** 022079
[275] Gritsenko V A, Kwok R W M, Wong H and Xu J B 2002 Short-range order in non-stoichiometric amorphous silicon oxynitride and silicon-rich nitride *J. Non-Cryst. Solids* **297** 96–101
[276] Kohli S, Theil J A, Dippo P C, Ahrenkiel R K, Rithner C D and Dorhout P K 2005 Chemical, optical, vibrational and luminescent properties of hydrogenated silicon-rich oxynitride films *Thin Solid Films* **473** 89–97
[277] Barranco A *et al* 2021 Understanding the role of defects in silicon nitride-based resistive switching memories through oxygen doping *IEEE Trans. Nanotechnol.* **20** 356–64
[278] Baik S J, Lim K S, Choi W, Yoo H and Shin H 2011 Charge diffusion in silicon nitrides: scalability assessment of nitride based flash memory *2011 Int. Reliability Physics Symp.* 6B.4.1–6B.4.6
[279] Vasileiadis N *et al* 2021 Understanding the role of defects in silicon nitride-based resistive switching memories through oxygen doping *IEEE Trans. Nanotechnol.* **20** 356–64
[280] Kapoor V J, Bailey R S and Smith S R 1981 Impurities-related memory traps in silicon nitride thin films *J. Vac. Sci. Technol.* **18** 305–08
[281] Xu D and Kapoor V J 1991 Effects of oxygen content and oxide layer thickness on interface state densities for metal-oxynitride-oxide-silicon devices *J. Appl. Phys.* **70** 1570–74
[282] Yeh J L and Lee S C 1996 Structural and optical properties of amorphous silicon oxynitride *J. Appl. Phys.* **79** 656–63
[283] Karakolis P, Normand P, Dimitrakis P, Sygelou L, Ntinas V, Fyrigos I A, Karafyllidis I and Sirakoulis G C 2019 Plasma modified silicon nitride resistive switching memories *2019 IEEE/ACM Int. Symp. on Nanoscale Architectures (NANOARCH)* pp 1–2
[284] Habraken F H P M and Kuiper A E T 1994 Silicon nitride and oxynitride films *Mater. Sci. Eng. R: Rep.* **12** 123–75
[285] Sorokin A N, Karpushin A A, Gritsenko V A and Wong H 2009 Electronic structure of amorphous silicon oxynitride with different compositions *J. Appl. Phys.* **105** 073706
[286] Ma H P, Lu H L, Yang J H, Li X X, Wang T, Huang W, Yuan G J, Komarov F F and Zhang D W 2018 Measurements of microstructural, chemical, optical and electrical properties of silicon-oxygen-nitrogen films prepared by plasma-enhanced atomic layer deposition *Nanomaterials* **8** 1008
[287] Perevalov T V, Volodin V A, Kamaev G N, Gismatulin A A, Cherkova S G, Prosvirin I P, Astankova K N and Gritsenko V A 2022 Electronic structure of silicon oxynitride films grown by plasma-enhanced chemical vapor deposition for memristor application *J. Non-Cryst. Solids* **598** 121925
[288] Mo C M, Zhang L, Xie C and Wang T 1993 Luminescence of nanometer-sized amorphous silicon nitride solids *J. Appl. Phys.* **73** 5185–88
[289] Liu Y, Zhou Y, Shi W, Zhao L, Sun B and Ye T 2004 Study of photoluminescence spectra of Si-rich SiN_x films *Mater. Lett.* **58** 2397–400
[290] Nguyen P D, Kepaptsoglou D M, Ramasse Q M, Sunding M F, Vestland L O, Finstad T G and Olsen A 2012 Impact of oxygen bonding on the atomic structure and photoluminescence properties of Si-rich silicon nitride thin films *J. Appl. Phys.* **112** 073514
[291] Jae-Young S *et al* 2021 Extraction of effective charge diffusivity in the charge trapping layer of sonos flash memory *Trans. Electr. Electron. Mater.* **22** 432–8
[292] Sandhya C *et al* 2009 Impact of SiN composition variation on SANOS memory performance and reliability under nand (FN/FN) operation *IEEE Trans. Electron Devices* **56** 3123–32
[293] Chen D, Huang S and He L 2017 Effect of oxygen concentration on resistive switching behavior in silicon oxynitride film *J. Semicond.* **38** 043002
[294] Novikov Y N, Kamaev G N, Prosvirin I P and Gritsenko V A 2023 Memory properties and short-range order in silicon oxynitride-based memristors *Appl. Phys. Lett.* **122** 232903
[295] Ermak K, Kamaev G and Volodin V 2025 Resistive switching and synaptic properties of Ni/SiOxNy/Si devices *2025 IEEE 26th Int. Conf. of Young Professionals in Electron Devices and Materials (EDM)* pp 70–73
[296] Grillo M E *et al* 2014 First-principles study of oxygen and aluminum defects in β-Si_3N_4: compensation and charge trapping *Comput. Mater. Sci.* **81** 178–83
[297] Bermudez V M 2020 First-principles study of electron trapping by intrinsic surface states on β-Si_3N_4 (0001) *Surf. Sci.* **691** 121511